Enhancing the mobility of small-scale robots via nonlinear structural springs exhibiting negative stiffness

Yujia Zhang[a,*], Jiajia Shen[b,*], Yao Yan[c,*], Jingzhong Tong[a], Lei Zhang[a,**], Yang Liu[b,**]

[a] *Institute of Advanced Engineering Structures, Zhejiang University, Hangzhou 310058, China*
[b] *Engineering Department, University of Exeter, North Park Road, Exeter, UK, EX4 4QF*
[c] *School of Aeronautics and Astronautics, University of Electronic Science and Technology of China, Chengdu, 611731, China*

Abstract

Compared to traditional robotic systems, small-scale robots, ranging from several millimetres to micrometres in size, are capable of reaching narrower and vulnerable regions with minimal damage. However, conventional small-scale robots' limited maneuverability and controlability hinder their ability to effectively navigate in the intricate environments, such as the gastrointestinal tract. Self-propelled capsule robots driven by vibrations and impacts emerge as a promising solution, holding the potentials to enhance diagnostic accuracy, enable targeted drug delivery, and alleviate patient discomfort during gastrointestinal endoscopic procedures. This paper builds upon our previous work on self-propelled capsule robots, exploring the potential of nonlinear connecting springs to enhance its propulsion capabilities. Leveraging a mathematical model for self-propelling robots with a *von Mises* truss spring, which is verified using a finite element model, we investigate the effects of negative stiffness and snap-back within the nonlinear structural spring on the robots' propelling speed. Our analysis reveals that the negative stiffness of the *von Mises* truss can significantly reduce the sensitivity of the propelling speed to excitation frequency. As a result, the capsule robot exhibits a remarkably wider operational band where it maintains a high average propelling speed, surpassing its linear counterpart. This work sheds light on the potential for developing customised nonlinear structural systems for diverse scenarios in small-scale robot applications, opening up new possibilities for enhanced functionality and maneuverability in various biomedical applications.

Keywords: Functionalised nonlinear structures; *von Mises* truss; Self-propelling robots; Structural dynamics; Elastic tailoring; Performance-based inverse design.

1. Introduction

Scientific advances in robot design and control offer exciting opportunities in various engineering sections, such as healthcare [1], energy [2], water [3] and food industry [4]. However, robotic engineers face enormous challenges in making robots robust enough to remain environmentally resilient and commercially competitive. This has led to their poor control performance due to the intrinsic or external nonlinearities caused by their mechanical structures or environmental interference, respectively. Small-scale robots [5], known as smaller-than-conventional robots, ranging from several millimetres to micrometres in size, fall into this category. They are of interest for applications that range from tools for minimally invasive surgical procedures in clinical medicine [6, 7]

*Co-first authors. These authors contributed equally to the work.
**Corresponding authors.
Email addresses: 22112036@zju.edu.cn (Yujia Zhang), j.shen3@exeter.ac.uk (Jiajia Shen), y.yan@uestc.edu.cn (Yao Yan), tongjz@zju.edu.cn (Jingzhong Tong), celzhang@zju.edu.cn (Lei Zhang), y.liu2@exeter.ac.uk (Yang Liu)

to flying robots for environmental exploration and manipulation [8]. As the size of the robot decreases, the physics that governs their modes of operation changes dramatically. In particular, the limited classes of structures and materials that can be used in such robots, however, create challenges in achieving desired performance and modes of operation. The limited force or torque outputs of miniature actuators and power deliveries constrain their performances and functionalities. Thus, novel engineering solutions for these robots to improve their performances (such as propelling speed) in terms of robustness and efficacy are timely and vital.

Compared to conventional robotic systems, small-scale robots are capable of reaching narrower and vulnerable regions with minimal damage. However, limited by their dimensions, microprocessors, power supplies, and sensors can hardly be integrated onboard. In addition, existing small-scale robots are characterised by slow propelling speeds and limited re-programmability (controllability) in their modes of operations [9]. In this paper, we will explore and exploit structural instability for enhancing the performance of small-scale robots. We will exemplify and demonstrate our proposed design on a self-propelled capsule robot [10, 11]. The robot experiences oscillations, frictions and collisions, with limited propulsive force due to its millimetre-scale dimension. Its dynamic characteristics [12] are typical in small-scale robots, which thus provides a rationale for using it as a benchmark system in the present work. In particular, we will show the significant improvement of its propelling speed by utilising the structural instability of a *von Mises* truss.

Structural instabilities, which were traditionally regarded as failure modes [13, 14], are recently exploited as a functionality or benefit, such as shape shifting in adaptive structures for lightweight design [15, 16], surface texturing [17, 18], advanced manufacturing of flexible electronics [19–21], fast response soft robots [22–25], mechanical metamaterials exhibiting distinct and programmable properties [26–29] and non-destructive structural testing technique [30–35]. These novel applications are known as *well-behaved nonlinear structures* [36] or *Buckliphilia* [37].

A key challenge in the broader application of *well-behaved nonlinear structures* lies in the absence of a robust analysis and design tool. Well-behaved nonlinear structures, due to their slender nature, often exhibit highly nonlinear behaviour or multistability [18, 24, 29, 36, 38]. Existing quasi-static nonlinear solvers in commercial finite element (FE) packages, such as Abaqus and Ansys, cannot efficiently and accurately explore the design space without prior knowledge of their bifurcation landscape. The generalised path-following algorithm [36, 39, 40], which can pinpoint critical points, switching branches, and trace equilibria with respect to third parameters, has demonstrated its capabilities in unveiling the complex nonlinear behaviour of compliant structures in a robust and efficient way [18, 29, 41]. However, there is still a need for the development of a user-friendly inverse design tool to complement existing methods. Recent advancements in machine learning algorithms and toolboxes, coupled with optimisation algorithms, have shown promise in addressing this need [28, 42–44]. These approaches enable the development of an efficient inverse design tool by leveraging trained machine learning models, which can significantly reduce the computational effort required for nonlinear analysis. To ensure the success of such a tool, high-quality training data is essential. On the other hand, training a robust machine learning model capable of describing the entire nonlinear equilibrium path of nonlinear structures remains a formidable challenge due to its high dimensionality [45]. Hence, an analytical model with a closed-form solution or one that can be efficiently solved using numerical methods remains a promising approach for the inverse design of 'well-behaved nonlinear structures', particularly in the initial design phase [16].

Owing to its simplicity, analytical solvability and programmable characteristic nonlinear response, *von Mises* truss has been widely used as a benchmark example to unveil the nonlinear mechanics of complex structural systems and develop novel techniques or design philosophy [31, 46–48]. In particular, Findeisen *et al.* [47] introduced a vertical spring in parallel connected with a *von Mises* truss. By varying the stiffness of the new added spring and the rise-span ratio, they produced a variety of different nonlinear behaviour from mono-stable or bi-stable behaviour. This model facilitates the design of the building blocks in mechanical metamaterials, contributing to enhanced energy dissipation capabilities. More recently, Neville *et al.* [31] further unveiled that *von Mises* truss can exhibit snap-backs, *i.e.* displacement limit points, when the apex of the truss

is connected in series with a vertical spring. This concept was implemented on a soft mechanical metamaterial both numerically and experimentally, where the snap-back behaviour tailored via fiber reinforcement [49]. Yang *et al.* [48] developed a *von Mises* truss with a tunable horizontal spring connecting its supports. By adjusting the spring's stiffness, they achieved a switchable behaviour between mono-stable and bi-stable responses in the *von Mises* truss. This mechanical design served as the foundation for their development of a shape memory metamaterial. Given their rich programmability and simplicity, we will utilise the *von Mises* truss as the nonlinear structural spring to replace the linear spring in the existing self-propelling capsule robot to tailor its driving performance.

In the authors' recent work [50], a comprehensive mathematical model was developed to describe the dynamic response of a self-propelling capsule robot integrated with a *von Mises* truss spring. Our findings demonstrated that by using the *von Mises* truss spring, the robot can achieve faster average propelling speeds than its linear spring counterpart under specific parameter regimes with restricted power inputs. The discovery addresses one of the key challenges for small-scale robots, where power input limitations pose a persistent obstacle. However, a comprehensive understanding of how the *von Mises* truss's nonlinearities influence the robot's propelling performance remains elusive.

This study delves deeper into this crucial gap, investigating the nuanced interplay between the nonlinear spring's mechanics and the robot's dynamics. By unraveling these complexities, we aim to unlock the full potential of the *von Mises* truss for propelling the next-generation small-scale robots with superior agility, efficiency and robustness. The rest of the paper is structured as follows. Section 2 defines the problem. Section 3 presents the mathematical model describing the nonlinear dynamic response of the capsule robot integrated with a *von Mises* truss spring. This section also details the verification of the mathematical model using finite element modelling. The numerical results obtained from the model are presented in Section 4, and further discussions are made in Section 5. Finally, conclusions are drawn in Section 6.

2. Problem description and *von Mises* truss

This study investigates a self-propelled capsule robot driven by a periodically actuated magnet (as a "hammer") within its core, as shown in Fig. 1(a). This unique configuration leverages the hammer-main body interaction as a propulsion mechanism, particularly during resonance, while overcoming external resistances encountered in diverse environments (*e.g.*, in the colon for bowel cancer screening [11]). While miniaturised capsule robots with electromagnetic actuation have been explored [51, 52], limitations in onboard or external coil-generated forces often hinder their locomotor performance. To address this, we depart from existing designs by replacing the conventional linear connecting spring in Fig. 1(b) with a nonlinear spring exhibiting negative stiffness or even snap-back behaviour. This study delves into the intricate interplay between this novel spring's mechanics and the capsule robot's propelling performance, paving the way for enhanced mobility in the challenging environments.

3. Method

3.1. Nonlinear mechanics of the von Mises *truss*

Figure 1(b2) presents a *von Mises* truss connected in series with linear springs. This structure features an arch-like arrangement of two inclined linear springs k_1, two vertical linear springs k_2 to provide vertical elastic constraint to the supports and a horizontal spring k_3 connecting the actuation point and the apex. The rise of the truss is H, and the span is L. The external loading is applied at the left end of the horizontal spring. The governing equation for this model can be found from the *Supplementary Materials*. Considering that the shell of the capsule robot is much stiffer than the support spring systems, we assume that $k_2 = \infty$ in the paper. Then the *von Mises*

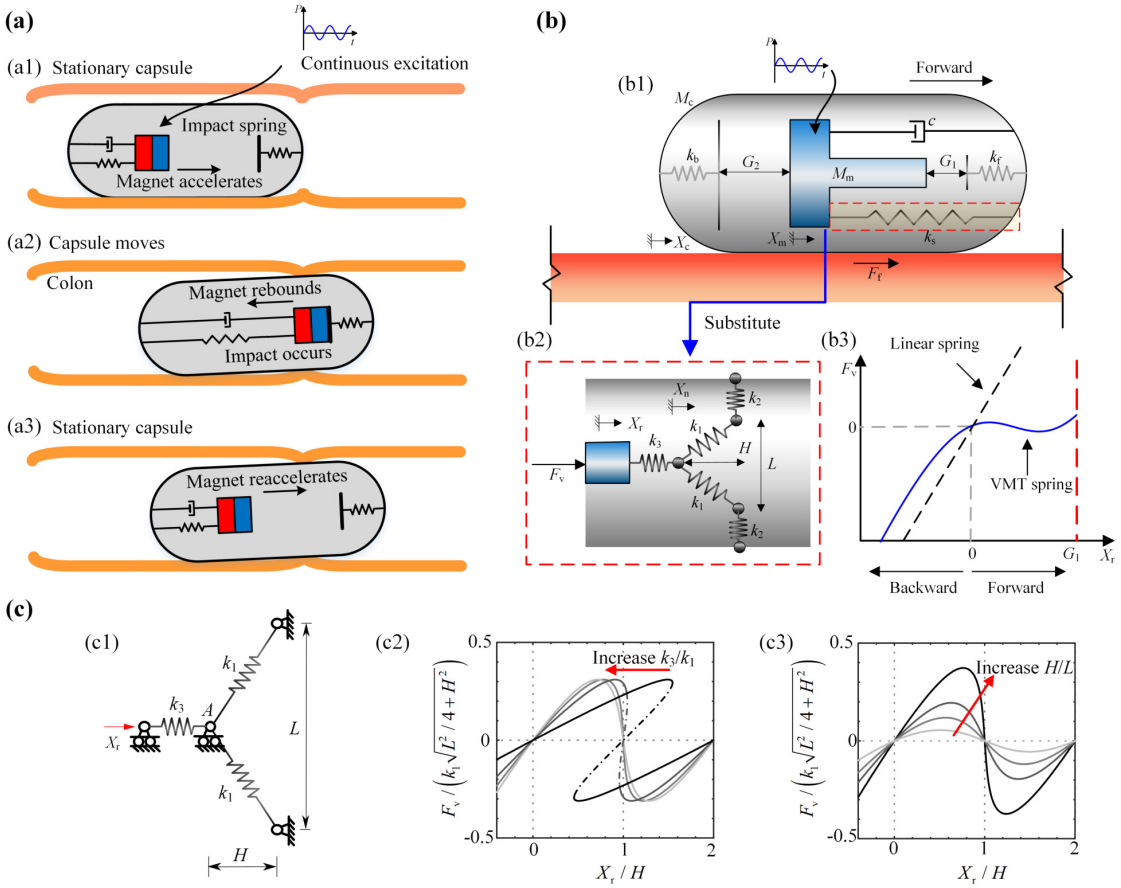

Figure 1: (Colour online) (a) Working principle of the self-propelled capsule robot for colon screening [11]: a permanent magnet attaching to a capsule via a conventional connecting spring is excited using an on-off electromagnetic field (sinusoidal wave) and collides with an impact spring intermittently. Once the resultant elastic force on the capsule is greater than the resistant force from the environment (the colon), the robot will move forward. (b) Physical model of the self-propelled capsule robot system integrated with a linear and a *von Mises* truss (VMT) connecting springs and their characteristic reaction force–relative displacement relationships. k_1, k_2 and k_3 are the stiffness of the inclined springs, vertical springs at the supports to control the span deformation and the horizontal spring at the loading point. Note that the VMT spring exhibits an asymmetric response to both compression and tension. (c) Simplified *von Mises* truss model with a fixed span L, *i.e.* set $k_2 = \infty$ in the VMT spring in subfigure b(2). Elastic tailoring of VMT spring by adjusting the stiffness properties (k_3/k_1) and geometry (H/L) to achieve a variety of different nonlinear behaviours.

truss model can be simplified as that in Fig. 1(c1). The governing equation of the simplified *von Mises* truss can be written as:

$$F_{\mathrm{v}} = \frac{2\,k_1 \left(L - \sqrt{L^2 - H^2 + \left(H - u_{\mathrm{apx}}\right)^2} \right) \left(H - u_{\mathrm{apx}}\right)}{\sqrt{L^2 - H^2 + \left(H - u_{\mathrm{apx}}\right)^2}}, \tag{1}$$

where u_{apx} is the horizontal displacement at the apex of the *von Mises* truss, *i.e.*, *Point A* in Fig. 1(c1). The horizontal displacement at the actuation point X_{r} can be written as

$$X_{\mathrm{r}} = \frac{F_{\mathrm{v}}}{k_3} + u_{\mathrm{apex}}. \tag{2}$$

The *von Mises* truss spring exhibits an asymmetric response to both compression and tension. By adjusting the rise-span ratio H/L as well as the stiffness ratio between the horizontal and

inclined springs k_3/k_1, a relatively rich behaviour, *i.e.* a variety of different initial stiffness, critical loads and snap-backs, can be obtained, as shown in Figs. 1(c2) and (c3). Note that a detailed exposition of the analytical model of the *von Mises* truss, the extensive parametric study, and the performance-based inverse design can be found from the *Supplementary Materials*.

3.2. Mathematical model development and solution technique

In this section, a relatively concise but self-contained introduction of the mathematical model describing the dynamic response of the self-propelling capsule robot with a *von Mises* truss spring and its solution method are presented, as shown in Fig. 1(b). A more detailed exposition can be found in the authors' work [50]. The capsule robot system, as depicted in Fig. 1(a), operates in bidirectional stick-slip phases comprising the following four modes: *stationary capsule robot without impact*, *moving capsule robot without impact*, *stationary capsule robot with impact*, and *moving capsule robot with impact*. All these modes can be modelled using the following equations of motion

$$\begin{cases} M_{\mathrm{m}}\ddot{X}_{\mathrm{m}} &= F_{\mathrm{e}} - F_{\mathrm{i}}, \\ M_{\mathrm{c}}\ddot{X}_{\mathrm{c}} &= F_{\mathrm{f}} + F_{\mathrm{i}}, \end{cases} \tag{3}$$

where F_{e} is the external excitation on the permanent magnet from an electromagnetic field, F_{f} is the friction acting on the capsule robot, and F_{i} represents the interaction force between the capsule and the magnet written as

$$F_{\mathrm{i}} = \begin{cases} F_{\mathrm{v}} + cv_{\mathrm{r}} + F_2, & X_{\mathrm{r}} \le -G_2, \\ F_{\mathrm{v}} + cv_{\mathrm{r}}, & -G_2 \le X_{\mathrm{r}} \le G_1, \\ F_{\mathrm{v}} + cv_{\mathrm{r}} + F_1, & X_{\mathrm{r}} \ge G_1. \end{cases} \tag{4}$$

Here, $X_{\mathrm{r}} = X_{\mathrm{m}} - X_{\mathrm{c}}$ and $v_{\mathrm{r}} = v_{\mathrm{m}} - v_{\mathrm{c}}$ represent the relative displacement and velocity between the magnet and the capsule. The interaction forces for the front and back constraints are represented by $F_1 = k_{\mathrm{f}}(X_{\mathrm{r}} - G_1)$ and $F_2 = k_{\mathrm{b}}(X_{\mathrm{r}} + G_2)$, respectively. The reaction force in the *von Mises* spring, as shown in Fig. 1(c1), can be written as

$$\begin{cases} F_{\mathrm{v}} = k_3\left(X_{\mathrm{r}} - X_{\mathrm{n}}\right), \\ F_{\mathrm{v}} = 2k_1\left(L - \sqrt{L^2 - H^2 + \left(H - X_{\mathrm{n}}\right)^2}\right)\frac{H - X_{\mathrm{n}}}{\sqrt{L^2 - H^2 + \left(H - X_{\mathrm{n}}\right)^2}}. \end{cases} \tag{5}$$

For any given relative displacement, X_{r}, the displacement of the node point and the force of the *von Mises* spring, X_{n} and F_{v}, can be obtained by numerically solving Eq. (5) using Newton-Rapson method. For some parameter combinations, the *von Mises* spring displays a hysteresis loop, as seen in Fig. 3(c). Namely, there is a region in the vicinity of $X_{\mathrm{r}} = H$ where F_{v} has two values for a given relative displacement.

In this study, the frictional force between the capsule robot and the supporting surface is given as

$$\begin{cases} F_{\mathrm{f}} \in [-P_{\mathrm{f}},\, P_{\mathrm{f}}], & v_{\mathrm{c}} = 0, \\ F_{\mathrm{f}} = -\mathrm{sign}(v_{\mathrm{c}})P_{\mathrm{f}}, & v_{\mathrm{c}} \neq 0, \end{cases} \tag{6}$$

where $P_{\mathrm{f}} = \mu(M_{\mathrm{m}} + M_{\mathrm{c}})g$ is the static friction of the capsule robot, and g is the gravitational acceleration. The external excitation, F_{e}, is a sinusoidal excitation written as

$$F_{\mathrm{e}}(t) = P_{\mathrm{d}}\sin(\Omega t), \tag{7}$$

where P_{d} and Ω are the amplitude and frequency of the excitation, respectively. The system and control parameters of the capsule robot used in the present study are summarised in Table 1.

3.3. Verification of the mathematical model using finite element model

To verify the mathematical model in the preceding section, we develop a 2-D plane stress finite

Table 1: System and control parameters of the capsule robot. Physical parameters of the robot were adopted from our previously reported prototype [52]. Physical parameters of the *von Mises* truss were selected based on the dimensions of our capsule robot prototype and the feasibility of fabricating such a truss in real-world scenarios.

Parameters	Unit	Values
Inner mass weight M_{m}	g	1.8
Capsule weight M_{c}	g	1.67
Friction coefficient μ	–	0.2293
Inclined spring of *von Mises* truss k_1	kN/m	[0,1000]
Horizontal spring of *von Mises* truss k_3	kN/m	0.062
Rise of the *von Mises* truss H	mm	[0.1,1.5]
Span of the *von Mises* truss L	mm	[0.1,1.5]
Forward constraint spring k_{f}	kN/m	53.5
Backward constraint spring k_{b}	kN/m	27.9
Magnitude of the excitation force P_{d}	mN	$[10, 80]$
Frequency of the excitation Ω	Hz	$[1, 50]$
Elastic modulus of inner mass E_{m}	GPa	200
Elastic modulus of capsule E_{c}	GPa	0.11
Mass density of inner mass ρ_{m}	g/cm^3	7.85
Mass density of capsule ρ_{c}	g/cm^3	0.95

element model in the commercial finite element package ABAQUS, as shown in Figure 2(a). The details of the FE model and the solution method can be found in Appendix A.

Figure 2(b) presents the displacement and velocity of the capsule robot within 0.05 seconds under the excitation force of 20 mN and frequency of 37 Hz, respectively. The key parameters of the *von Mises* truss spring are: $k_1 = 0.368$ kN/m, $k_3 = 1000$ kN/m, $H = 0.289$ mm, and $L = 0.911$ mm. The other system and control parameters are presented in Table 1. For better visualization, the deformation configurations of the capsule robot from the FE simulation at selected states are shown in Figure 2(c). An excellent agreement is observed between the results obtained from the finite element model and the mathematical model. While both models provide valuable insights, the mathematical model offers a significant advantage in computational efficiency. To illustrate this, consider a simulation of the first ten cycles. On an Intel(R) Core(TM) i7-10870H processor, the mathematical model takes only 13.68 seconds, whereas the FE model requires 4759 seconds (over 82 minutes). This translates to a remarkable 350 times faster computation with the mathematical model.

Based on this comparison, we can confidently conclude that the developed mathematical model has been successfully verified against the FE model. This verification demonstrates that the mathematical model captures the essential behaviors of the capsule robot with sufficient accuracy for preliminary design purposes. The mathematical model is now ready for further applications.

4. Results

With the integrated mathematical model, we conduct an extensive parametric study on how the nonlinearity of the *von Mises* spring system affects the propelling performance of the capsule robot. In particular, we select the average effective propelling speed $v_{\mathrm{pro,avg}}$ as the key performance index. Each simulation was conducted for a total of 60 driven periods of sinusoidal excitation. To eliminate the transient effects associated with the initial transient phase, the first 40 periods were discarded. The average propelling speed $v_{\mathrm{pro,avg}}$ was then calculated by dividing the total propelling displacement of the robot over the last 20 periods by the elapsed time. For simplicity, we assume that both the initial displacement and speed are zero. Additionally, we consider the initial net gaps, G_1 and G_2, to be equal. Note that the scope of parameters considered in this parametric study is intentionally limited. This approach is designed to reveal the fundamental mechanics governing the interaction between the nonlinear spring and the system as a whole. A comprehensive parametric analysis, encompassing all parameter regimes of practical significance, is earmarked for subsequent research endeavors.

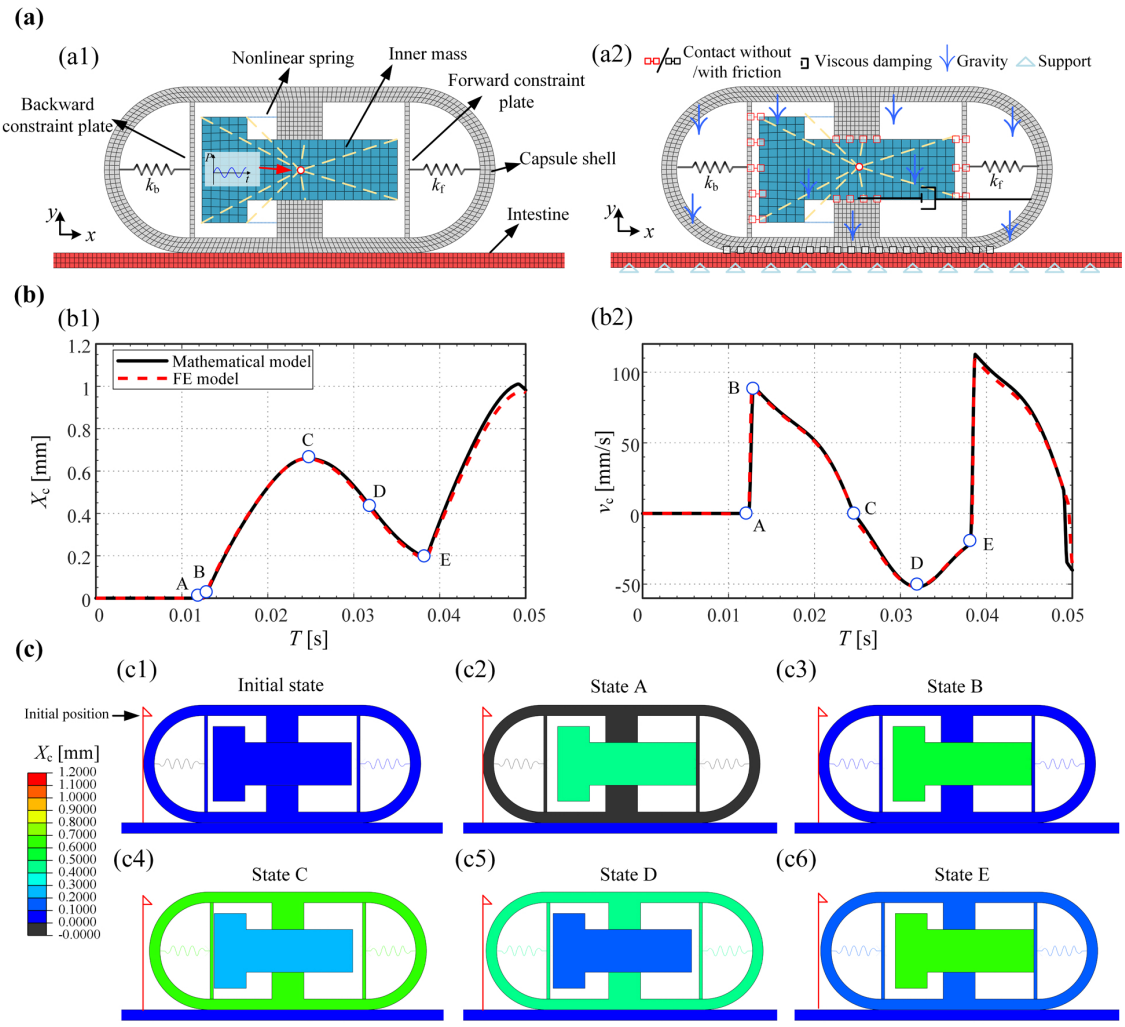

Figure 2: (a) Illustration of the FE model for capsule robot developed in ABAQUS. Note that the *von Mises* truss spring is modelled using a pair of axial connectors that exhibit an identical force–displacement relationship as the *von Mises* truss. (b) Time history for the displacement and velocity of the capsule robot under the excitation force $P_d = 20$ mN and the frequency $\Omega = 37$ Hz. The stiffness and geometric properties of the *von Mises* are $k_1 = 0.368$ kN/m, $k_3 = 1000$ kN/m, $H = 0.289$ mm, and $L = 0.911$ mm. All the other parameters of the capsule robots are presented in Table 1. (c) Deformation configurations of the capsule robot at selected states within the first excitation cycle. The red flag represents the initial position of the capsule.

As shown in Table 1, the stiffness of the forward and backward constraint springs is significantly larger than that of the supporting spring k_s connected to the mass. Therefore, when the mass contacts with the constraint springs, the reaction force applied to the mass will be mainly provided by the constraint springs. The effective working regime for the *von Mises* spring will be the net distance G_1. In this study, G_1 is set based on the parametric study on the performance of a capsule robot with a linear connecting spring k_s, as shown in Fig. 1(b). The details of the parametric results can be found in the *Supplementary Materials*. We found that with the excitation frequency and amplitude being 29 Hz and 30 mN, the combination of $G_1 = 0.5$ mm and $k_s = 0.025$ kN/m, leading to the fastest average propelling speed $v_{pro,avg}$. Therefore, we set $G_1 = 0.5$ mm as the net distance of the capsule robot throughout our analysis.

4.1. Effects of negative stiffness

Referring to Fig. 1(c) and the governing equations Eqs. (1) and (2), the mechanical performance indices of the *von Mises* truss, *i.e.* the initial tangential stiffness $k_{\mathrm{int,T}}$, the force and displacement at the critical point $F_{\max}$ and $X_{\mathrm{r,max}}$, are coupled. Changing one index would lead to the change of the other indices. To understand the effects of each factor on the response of the robot, we adopt a step-by-step approach, where only one parameter is studied at one time. For simplicity, we start with the case that the horizontal spring k_3 is rigid, *i.e.* $k_3 \to \infty$, such that there is no snap-back in its nonlinear equilibrium path.

The case with the linear connecting spring yielding the highest propelling speed, *i.e.* $G_1 = 0.5$ mm, and $k_{\mathrm{s}} = 0.025$ kN/m, is selected as the reference baseline state. We set the initial tangential stiffness of the *von Mises* truss identical to the stiffness of the linear spring, *i.e.* $k_{\mathrm{ini,T}} = 0.025$ kN/m. The corresponding geometry and material properties for *von Mises* trusses are solved using a performance-based inverse design framework based on optimisation, which can be found in Supplementary Materials.

We select four characteristic *von Mises* truss nonlinear springs in the parametric study, as shown in Fig. 3(a). They exhibit identical initial tangent stiffness but with different characteristic points locating at $X_{\mathrm{r}}/G_1 = 1$, *i.e.* when the inner mass collides with the capsule:

- Case 1: the snap-through point with $F_{\mathrm{v}} = F_{\max}$ locates at $X_{\mathrm{r}} = G_1$;
- Case 2, the local minimum with $F_{\mathrm{v}} = -F_{\max}$ locates at $X_{\mathrm{r}} = G_1$;
- Case 3, the transitional unstable equilibrium with $F_{\mathrm{v}} = 0$ locates at $X_{\mathrm{r}} = G_1$;
- Case 4, the local maximum with $F_{\mathrm{v}} = F_{\max}$ locates at $X_{\mathrm{r}} = G_1$.

Under the constraint of identical tangential stiffness, the stiffness of the four cases also exhibits opposite trends for $X_{\mathrm{r}} > 0$ and $X_{\mathrm{r}} < 0$, respectively. For instance, when $X_{\mathrm{r}} > 0$, the stiffness of case 1 exhibits the most pronounced softening due to nonlinearity. Conversely, when $X_{\mathrm{r}} < 0$, it stiffens most significantly.

Figure 3(b) presents the average propelling velocity of the capsule robots with the four different types of *von Mises* truss springs under the excitation force $P_{\mathrm{d}} = 20$ mN in the frequency domain [0 50] Hz. Generally, in all four cases, the average propelling velocity $v_{\mathrm{pro,avg}}$ exhibits sensitivity to the excitation frequency, particularly in the low frequency high domain [0 20] Hz, where the direction and the magnitude of $v_{\mathrm{pro,avg}}$ can change sharply in an irregular way. In these regime, the inner mass exhibit a chaotic response under the excitation, thus leading their irregular velocity variation. More details can be found in the Supplementary Materials. Compared with case 4, where the *von Mises* truss exhibit no negative stiffness under compression, the other three cases exhibit a relatively high $v_{\mathrm{pro,avg}}$ in a relatively wide excitation frequency domain. This implies that the dynamic systems with the negative stiffness spring exhibit a more robust performance.

Figure 3(c) presents the detailed phase diagram and time history results corresponding to highest average propelling velocity for the each capsule. Subfigures 1 (first row) represent the phase portraits describing the relative velocity of the inner mass at different relative locations in the capsule for five periods. The overlap of the phase portraits for each case implies that the inner masses exhibit a periodic response. In all case, the inner mass collides with the front constraint spring (dashed red line at $X_{\mathrm{r}}/G_1 = 1$) but do not contact with the back constraint spring, leading to a higher propelling efficiency of the capsule robot. The net distance between the inner mass and the back spring decreases gradually from case 1 to case 4. Moreover, the left end of the phase portrait, which depicts the velocity deceleration rate pattern, transitions from a round shape to a sharp one. This aligns with the stiffness stiffening pattern of the *von Mises* truss springs across cases 1 to 4 (see Fig. 1(a)). It implies that we could adopt a stiffening spring in tension and a softening spring in compression to achieve a higher forward propelling speed for the capsule robot. Subfigures 2 and 3 (second and third rows in (c)) present the absolute displacement and velocity of the inner mass and the capsule robot within a single period. Note the displacements of the capsule and inner mass for a single period in case 4 are larger than those in other cases. However,

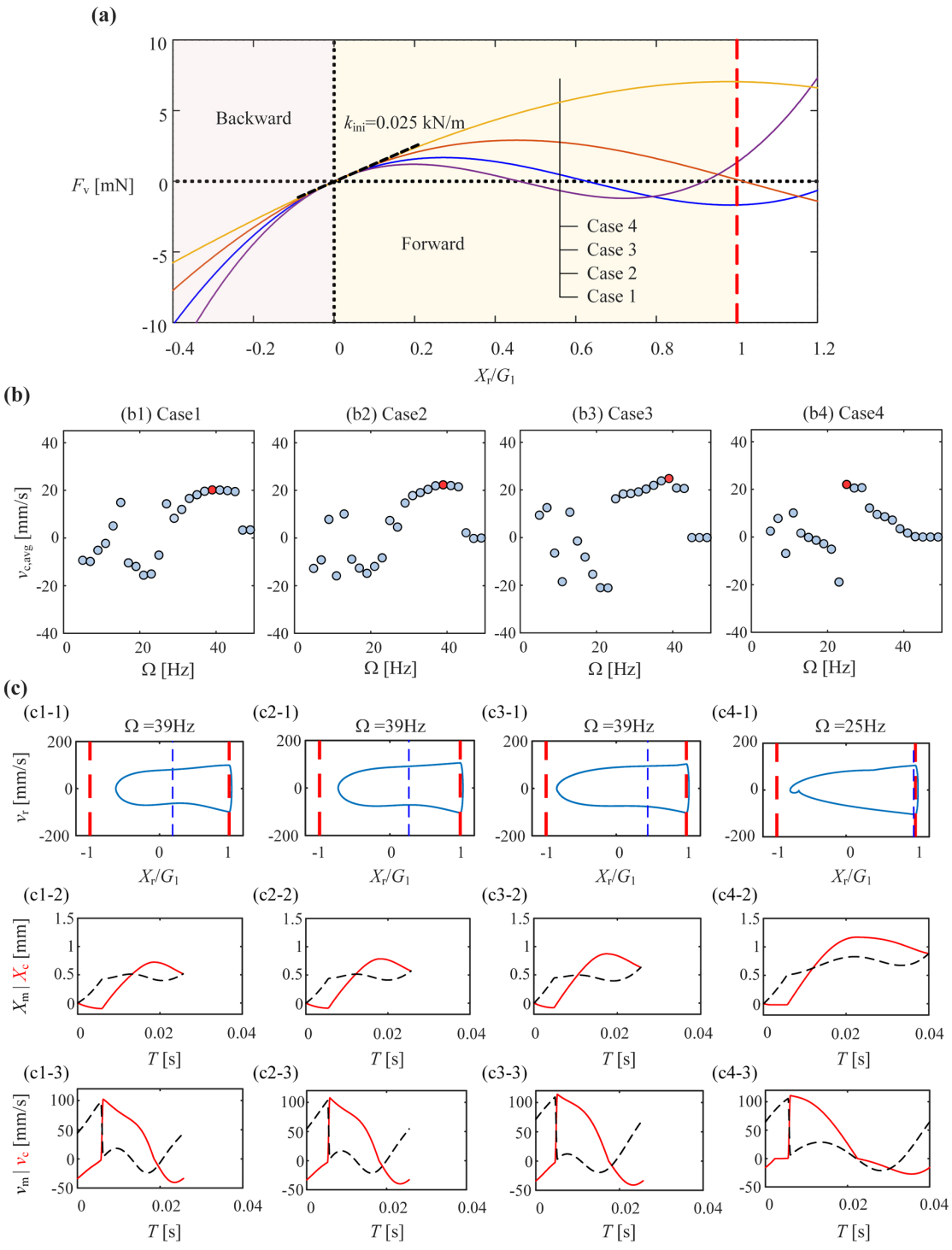

Figure 3: The average propelling speed of the capsule robots with the *von Mises* truss springs with identical tangent stiffness but different rises and peak loads. (a) Nonlinear equilibrium paths of the three characteristic *von Mises* trusses. (b) Average propelling speed of the capsule under the excitation force amplitude P_d = 20 mN in the excitation frequency ranging from 0 to 50 Hz. (c) The phase portraits and time history results of the capsule robots exhibiting highest average propelling velocity in (b). First row presents the relative velocity of the inner mass at different positions in a period of excitation circle. The thick red dashed red lines represent the front and back constraint springs. The thin blue dashed lines represent the force limit point, *i.e.* the starting point of the negative stiffness. The second and third rows present the time history for the displacement and velocity of the capsule robot (red solid curve) and the inner mass (black dashed curve) for a single period.

the period of case 4 is almost twice of the other three cases. Therefore, their average speed is almost identical.

The displacement and velocity diagrams vividly illustrate the working mechanics of the capsule robot. In these diagrams, both the displacement and velocity time histories begin at the state where the *von Mises* truss is stress-free, denoted by $X_\mathrm{r} = X_\mathrm{m} - X_\mathrm{c} = 0$. Initially, the inner mass and capsule moves in the opposite direction. When their relative displacement reaches the net distance between the inner mass and front panel, *i.e.* $X_\mathrm{r} = G_1$, collision occurs. This corresponds to the first sharp turning point on the displacement history curves and the the abrupt jump in the velocity history curve. After the collision, the inner mass and the capsule move in the same direction but the capsule moves much faster than the inner mass. As a result, the inner mass returns to 'origin' (the *von Mises* truss is stress-free), which corresponds to the cross of the displacement curves. Note that the velocity of the capsule v_c keeps decreasing after the collision and finally becomes negative. The transition point with $v_\mathrm{c} = 0$ corresponds to the peak of the displacement curve for the capsule. After that, the capsule moves backwards until the next collision. Note that the displacement and velocity time history diagrams for case 4 have some differences from cases 1–3, the latter of which are very similar. The capsule robot almost remains stationary instead of moving backward before its collision with the inner mass. This is because the reaction force applied on the capsule from the *von Mises* truss is not sufficiently large to overcome friction.

From the results in this section, we could conclude that the negative stiffness of the *von Mises* truss make the overall capsule robot less sensitive to the excitation frequency. Note that we also conducted a sensitivity study on cases with identical scant stiffness. They show similar trends as the case with the initial tangent stiffness. More detailed information could be found in Supplementary Materials.

4.2. Effects of initial stiffness and snap-back

In this section, we investigate the effects of initial tangential stiffness as well as the snap-back behaviour of the *von Mises* truss on the propelling performance of capsule robots. This is achieved by varying the stiffness of the horizontal spring k_3. In particular, we set the case 2 *von Mises* truss introduced in the previous subsection as the baseline, where the local minimum locates at $u_\mathrm{a} = G_1$. Figure 4(a) presents four characteristic nonlinear equilibrium path of the connecting *von Mises* truss spring with different k_3. The critical load F_max remains constant. The snap-back behaviour becomes more severe as the parameter k_3 decreases, while the initial stiffness concurrently decreases. The excitation force is set as $P_\mathrm{d} = 20$ mN. A sensitivity study on the excitation frequency is also conducted to identify the periodic response of the inner mass that leads to the maximum average propelling speed of the capsule robot.

As shown in Fig. 4(b), the maximum average propelling speed $v_\mathrm{pro,avg}$ of the capsule robot almost remains constant with the varying k_3. However, the sensitivity of $v_\mathrm{pro,avg}$ to the excitation frequency increases as k_3 decreases. For illustration purposes, the phase portraits and time history results of the dynamic behaviour of the inner mass and capsule robots with the highest average propelling velocity are presented in Fig. 4(c). From the phase portrait, the inner mass begins to collide with the back constraint spring as k_3 decreases. This behaviour aligns with the expected reduction in the stiffness of *von Mises* truss in both compression and tension drops as k_3 decreases. Moreover, the behaviour of the inner mass also transitions from periodic to aperiodic. This may explain their increased sensitivity to the excitation frequency. The detailed time history results for the displacement and velocity of the inner mass and the capsule are presented in the second and third rows of Fig. 4(c). Within the period, three collisions for case 1 (one for front panel and two for back panel), two collisions for cases 2 and 3 (one for front panel and the other one for back panel), and one collision for case 4 (only the front panel). Prior to the first collision, the capsules in cases 1–3 have zero velocity and remain stationary. This is attributed to the relatively small stiffness on the tension side of the *von Mises* truss, where the reaction force applied on the capsule is insufficient to overcome the friction force. As the stiffness on the tension side increases such that the applied force on the capsule surpasses the friction force, the capsules start moving backward before the collision, as that in case 4.

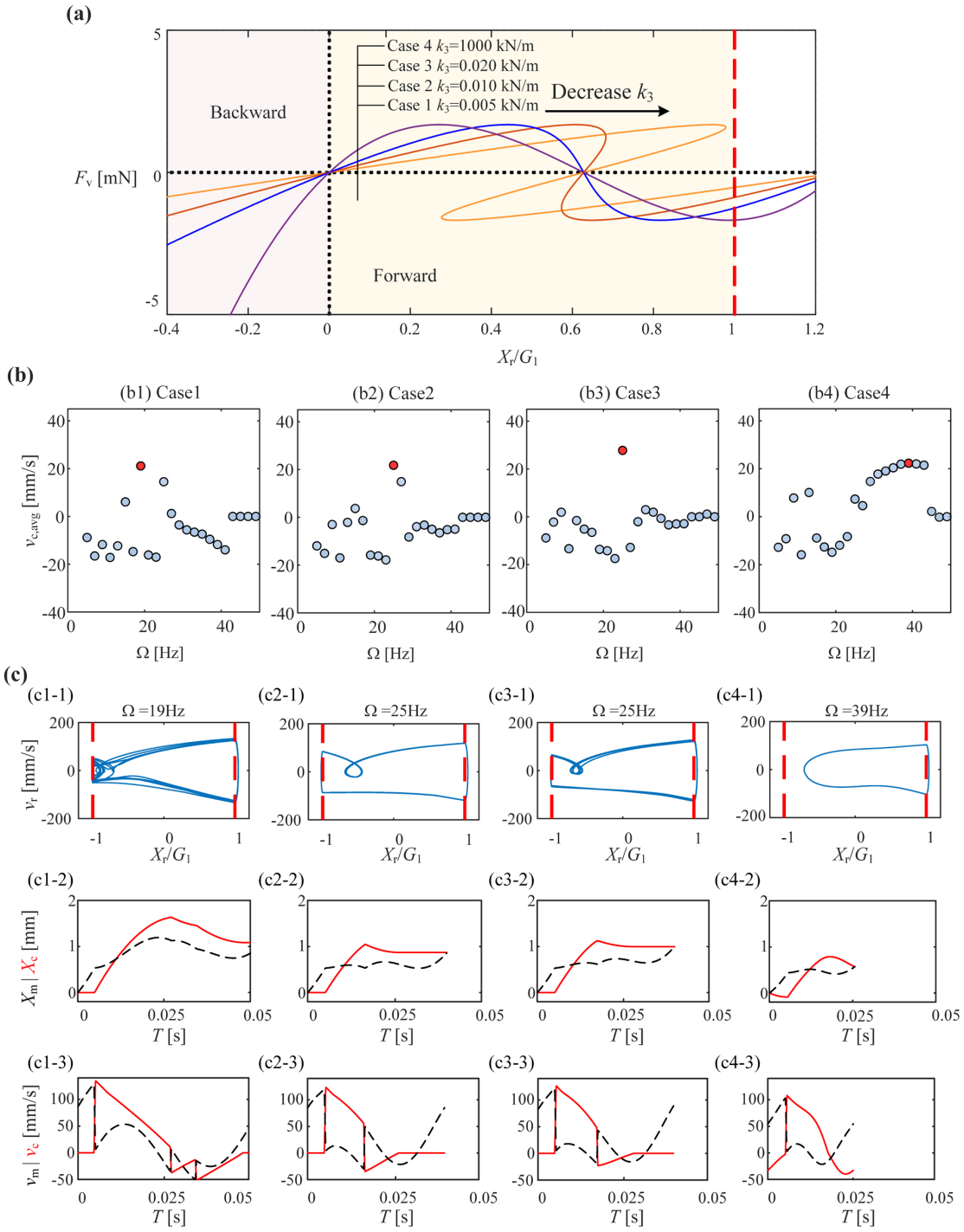

Figure 4: The average velocity of the capsule robots with the *von Mises* truss with different horizontal spring stiffness k_3. (a) Equilibrium paths of the *von Mises* trusses with different k_3. (b) The average propelling velocity of the capsule robots with different *von Mises* trusses with the excitation force $P_d = 20$ mN. (c) Phase portraits and time history results for the displacement and velocity of the inner mass and the capsule robots with the highest average speed for each case (red dots in (b)). Subfigures are as described in Fig. 3.

From the section, we could conclude that the snap-backs in the nonlinear spring would not improve the performance of the capsule robot. Moreover, to make the capsule robot move forward efficiently, we could design to make the *von Mises* truss spring stiffer under tension so that the inner mass would not collide with the back panel and the energy efficiency of the system would be much higher. Building upon the parametric study, we performed a mass-constrained optimization of the *von Mises* truss, achieving high propelling speeds across a broader frequency domain. Details of the optimized designs and further analyses are provided in the Supplementary Materials.

5. Discussion

This work provides another compelling example of 'well-behaved nonlinear structures' [36], wherein structural instability is harnessed for functional purposes. Much of the earlier research on well-behaved nonlinear structures primarily revolved around scenarios where these nonlinear structures operated independently to achieve desired functionalities [15, 22, 29, 53]. However, in this particular example, the nonlinear structure is seamlessly integrated into a complex system as a fundamental component. Assessing their performance for functionality necessitates the analysis of the overall system using the dynamic analysis, which is a more complex endeavor, often requiring interdisciplinary collaboration. This presents a new and exciting design paradigm and research avenue for exploring the potential of well-behaved nonlinear structures.

Unlike a linear spring, the *von Mises* truss exhibit distinct responses under compression and tension. While its behaviour remains nearly linear under tension, it becomes highly nonlinear during compression, displaying both positive and negative stiffness. This asymmetry in response contributes to the boost in the propelling speed of capsules. Note that we have demonstrated that the nonlinear spring systems can boost the performance of the self-propelling capsule robots via *von Mises* truss through analytical modelling and numerical continuation techniques. However, *von Mises* truss is not easy for manufacturing and minimization [54]. Pin linkages connecting the component springs can complicate the internal structure of the capsule robot. This complexity can hinder core functionalities like drug loading capacity and potentially pose challenges for the maintenance. Therefore, our future research will shift its focus towards the development of continuum nonlinear structures, such as shallow arches, domes [24], or origami [55], which have much simpler geometry but can also achieve the desired nonlinear response characteristics. By integrating these nonlinear continuum structures with additive manufacturing, we can develop a scale-independent nonlinear 'spring systems' with better performance. Furthermore, our current study concentrates solely on substituting the supporting spring with a nonlinear structured spring. Subsequent investigations could extend to replacing the two constraint springs, namely k_{f} and k_{b} in Fig. 1(a), with nonlinear structured springs. Given that they are already in the form of continuum structures [56], the replacement process is comparatively more straightforward. However, considering the computational efficiency of the *von Mises* truss model, it can be used as an inter-media for the analysis. More specifically, the performance-based inverse design process, which involves determining the specific structural form based on the desired nonlinear equilibrium path, can be carried out at the substructure level to enhance computational efficiency. Meanwhile, the evaluation of the robot's performance is conducted at the entire structure level using the *von Mises* truss model.

As for the *von Mises* truss model, it can exhibit a variety of different nonlinear behaviour by varying the stiffness of the component springs and the geometry. However, their nonlinear equilibrium path is centrosymmetry about the equilibrium state ($X_{\mathrm{r}} = H$, $F_{\mathrm{v}} = 0$). To further generalize the nonlinear response of the nonlinear spring, additional spring elements could be introduced in the *von Mises* truss, such as rotational springs mimic the bending stiffness between two inclined springs at the apex [16] or translational supporting spring at the apex [47] to make the *von Mises* truss exhibit mono-stable response. Additionally, exploring the concept of 'building blocks' [16], where distinct nonlinear substructures with characteristic bifurcation properties are combined, holds the potential to yield richer and more diverse nonlinear equilibrium paths. This approach has been demonstrated to potentially addresses some conflicting requirements [16], which otherwise cannot be satisfied using a single type of nonlinear structures.

In this study, our analysis is exclusively focused on the forward propulsion of the capsule robot. However, it is essential to note that the *von Mises* truss spring is bistable. Consequently, by applying an external stimulus to induce a mode switch from one stress-free state to another, the capsule could achieve enhanced speed in both forward and backward directions, as illustrated in Fig. 5. Furthermore, considering the net distance requirements for both directions, the mode switch could be accomplished by adjusting the position of the supports, as illustrated in Fig. 5. The detailed implementation of this concept will be explored in future work.

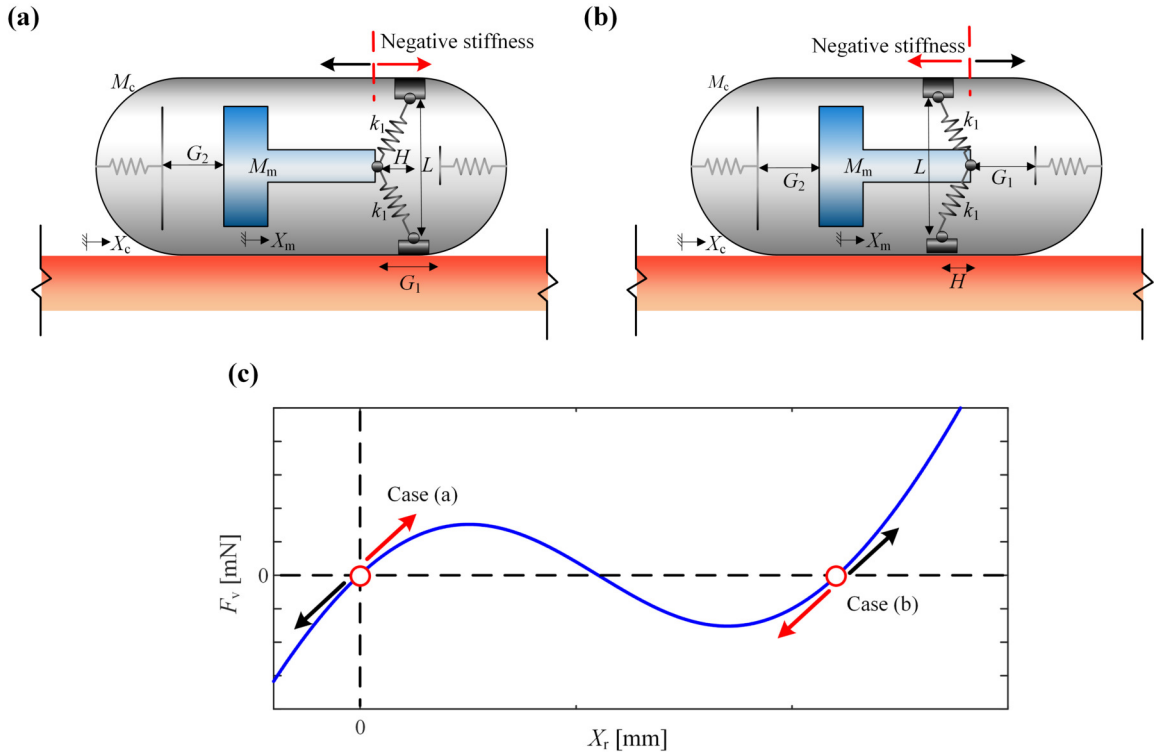

Figure 5: The two stable stress-free states of a *von Mises* truss and their characteristic reaction-force displacement relationship under compression and tension. In configurations (a) and (b), *von Mises* truss exhibit negative stiffness in the forward and backward directions, respectively. By switching between the two stable states, the capsule robot can achieve speed acceleration in both directions.

While this work focuses on the capsule's motion in a two-dimensional scenario, practical application within the complex gastrointestinal tract environment necessitates a broader range of maneuverability. Our future efforts will focus on developing a three-dimensional model incorporating novel re-programmable functionalized nonlinear structural elements. These elements, embedded with active materials (as explored by Qi *et al.* [57]), will possess the ability to dynamically modify their response upon external stimuli. This could potentially improve the maneuverability over the capsule robot, paving the way for achieving a degree of 'physical intelligence' [58] within the small-scale robot.

6. Conclusion

In this paper, we present a preliminary study on the integration of nonlinear structural spring systems with self-propelling capsule robots to enhance their propulsion performance. We exploited a finite element-verified mathematical model, which describes the dynamic response of self-propelling capsule robots integrated with *von Mises* truss, to unveil how the negative stiffness and the snap-back in the nonlinear equilibrium path of the *von Mises* truss affect the propelling

performance of capsule robots. We identified that the negative stiffness in the *von Mises* truss spring significantly reduces the sensitivity of the propelling speed to excitation frequency. As a result, the capsule robot exhibits a remarkably wider operational band where it maintains a high average propelling velocity, surpassing its linear counterpart and these exhibiting snap-back.

This study sheds light on the integration of *well-behaved nonlinear structures* with dynamic systems as a means to tailor the overall system performance. In future research, our focus will shift towards the development of size-independent and more readily manufacturable continuum nonlinear structures. These continuum structures are intended to replace the current *von Mises* truss system. A prototype robot will be manufactured and tested to substantiate the efficacy of this innovative design approach.

Authors' contributions

YZ: Data curation, Formal analysis, Investigation, Visualization, Software; **JS**: Conceptualization, Project administration, Investigation, Formal analysis, Methodology, Visualization, Supervision, Writing - original draft, review&editing; **YY**: Methodology, Software, Funding acquisition, Writing - review&editing; **JT**: Project administration, Resources, Supervision, Funding acquisition, Writing - review&editing; **LZ**: Project administration, Resources, Supervision; **YL**: Conceptualization, Project administration, Methodology, Resources, Software, Supervision, Funding acquisition, Writing - original draft, review&editing.

Acknowledgements

JS was funded by the Research Fellowship from Exeter Technologies Group at the University of Exeter. YY received funding from National Natural Science Foundation of China (Grant No. 12072068) and Sichuan Science and Technology Program (Grant No. 2022JDRC0018 and 2021ZDZX0004). JT received funding from National Natural Science Foundation of China (Grant No. 52108180) and Zhejiang Provincial Natural Science Foundation in China (Grant No. LR24E080002).

Competing interests

The authors have no relevant financial or non-financial interests to disclose.

Data accessibility

The datasets generated and analysed during the current study are not publicly available due to the potential use for further publications, but are available from the corresponding author on reasonable request.

Appendix A. Finite Element Model Development

The FE model in Figure 2(a) is designed to replicate the mathematical model by adhering to the following key principles:

1. The inner mass can only move along the horizontal direction without any rotation or deflection.
2. The inner mass, forward and backward constraint plate as well as the capsule shell as set as rigid body to avoid any elastic deformation.
3. All the surface are smooth except the interface between the capsule shell and the supporting ground.

Appendix A.1. Choice of element type and mesh scheme

The overall capsule shell, constraint plates, inner mass and supporting ground are discretised using four-node plane stress element with reduced integration (CPS4R) elements. The thicknesses of the CPS4R elements are determined based on the density and sectional area of the inner mass and the capsule, respectively. The density and stiffness properties of the materials are presented in Table 1. Based on the mesh sensitivity study in authors' previous study [56], the mesh sizes of the capsule, inner mass and intestine are taken as 0.3, 0.6 and 0.3mm, respectively.

The front and backward constraint springs k_{f} and k_{b} are modelled using 2-node linear spring element `Spring2`. For simplicity, the *von Mises* spring is modelled using a pair of axial connector elements `CONN2D2` with a user-defined force–displacement relationship derived from Eq. (2) using the corresponding parameters.

The viscous damping effect between the inner mass and capsule is modelled using the `Dashpots` element. This element connects the capsule shell and the inner mass. The damping coefficient (0.0156 Ns/m) is identical to that in the mathematical model.

Appendix A.2. Contact modelling, loading and boundary conditions

Contact interactions play an important role in the FE model. Here, we adopt two different strategies for modeling these interactions:

- Inner Mass and Capsule: To exclude frictional losses between the inner mass, capsule shell, and constraint plates, we utilize separable 'hard contact' in the normal direction and 'frictionless' behavior in the tangential direction.
- Intestine and Capsule: 'Hard contact' in the normal direction is used for the interaction between the intestine and the bottom edge of the capsule. Additionally, a friction behavior based on the penalty function with a friction coefficient is applied in the tangential direction. Here, the friction coefficient is 0.2293. This strategy ensures consistency with the mathematical model's friction behavior represented by Eq. (6).

As for the loading, the gravity effects and the excitation force are considered. A sinusoidal excitation load is applied on a reference point defined on the inner mass directly, as shown in Figure 2(a1).

To restrict movement and ensure desired behavior, two boundary conditions are applied:

- Intestine (supporting ground): All degrees of freedom on the bottom edge of the intestine are fixed.
- Capsule and Inner Mass: The vertical movement ($U2$ degree of freedom) of the capsule and inner mass is constrained, allowing them to move only in the horizontal direction ($U1$ degree of freedom).

Appendix A.3. Solution procedure

Here, a two-step analysis procedure is adopted. The first analysis step is to apply the gravity to the capsule robot using the `*Static` solver. The second step is the dynamic analysis to trace the dynamic response of the capsule robot under the excitation force. The implicit dynamic analysis using direct integration technique is adopted, *i.e.* `*Dynamic, direct` solver.

Appendix A.4. Limitations and future work

In this study, both the mathematical and FE models developed are intended as preliminary design tools. Their primary purpose is to provide a qualitative understanding of the capsule robot's behavior. To achieve a more precise representation of real-world scenarios, particularly regarding interactions with the environment, further refinement of the FE model is necessary. This refinement will be explored in future studies.

References

[1] A. Maibaum, A. Bischof, J. Hergesell, and B. Lipp, "A critique of robotics in health care," *AI & Soc.*, vol. 37, pp. 467–477, 2022.

[2] L. Yu, E. Yang, P. Ren, C. Luo, G. Dobie, D. Gu, and X. Yan, "Inspection robots in oil and gas industry: a review of current solutions and future trends," in *25th International Conference on Automation and Computing (ICAC)*, (Lancaster, UK), pp. 1–6, 2019.

[3] J. Aitken, M. Evans, R. Worley, S. Edwards, R. Zhang, T. Dodd, L. Mihaylova, and S. Anderson, "Simultaneous localization and mapping for inspection robots in water and sewer pipe networks: a review," *IEEE Access*, vol. 9, pp. 140173–140198, 2021.

[4] L. Duong, M. Al-Fadhli, S. Jagtap, F. Bader, W. Martindale, M. Swainson, and A. Paoli, "A review of robotics and autonomous systems in the food industry: From the supply chains perspective," *Trends in Food Science & Technology*, vol. 106, pp. 355–364, 2020.

[5] Y. Liu, F. Chernousko, B. Terry, and J. Páez Chávez, "Special issue on self-propelled robots: from theory to applications," *Meccanica*, vol. 58, pp. 317–319, 2022.

[6] W. Hu, G. Lum, M. Mastrangeli, and M. Sitti, "Small-scale soft-bodied robot with multimodal locomotion," *Nature*, vol. 554, pp. 81–85, 2018.

[7] S. Jeon, A. Hoshiar, K. Kim, S. Lee, E. Kim, S. Lee, J. Kim, B. Nelson, H. Cha, B. Yi, and H. Choi, "A magnetically controlled soft microrobot steering a guidewire in a three-dimensional phantom vascular network," *Soft Robotics*, vol. 6, pp. 54–68, 2019.

[8] Y. Chen, H. Zhao, J. Mao, P. Chirarattananon, E. Helbling, N. Hyun, D. Clarke, and R. Wood, "Controlled flight of a microrobot powered by soft artificial muscles," *Nature*, vol. 575, pp. 324–329, 2019.

[9] J. Jiang, Z. Yang, A. Ferreira, and L. Zhang, "Control and autonomy of microrobots: recent progress and perspective," *Adv. Intell. Syst.*, vol. 4, p. 2100279, 2022.

[10] Y. Liu, J. Páez Chávez, J. Zhang, J. Tian, B. Guo, and S. Prasad, "The vibro-impact capsule system in millimetre scale: numerical optimisation and experimental verification," *Meccanica*, vol. 55, pp. 1885–1902, 2020.

[11] J. Zhang, Y. Liu, J. Tian, D. Zhu, and S. Prasad, "Design and experimental investigation of a vibro-impact capsule robot for colonoscopy," *IEEE Robotics and Automation Letters*, vol. 8, pp. 1842–1849, 2023.

[12] Y. Shan, Y. Yan, J. Páez Chávez, and Y. Liu, "Dynamics of a self-propelled capsule robot in contact with different folds in the small intestine," *Communications in Nonlinear Science and Numerical Simulation*, vol. 126, p. 107445, 2023.

[13] Z. P. Bažant, "Structural stability," *International Journal of Solids and Structures*, vol. 37, no. 1-2, pp. 55–67, 2000.

[14] J. Shen and M. A. Wadee, "Length effects on interactive buckling in thin-walled rectangular hollow section struts," *Thin-Walled Structures*, vol. 128, pp. 152–170, 2018.

[15] G. Arena, R. M. J. Groh, A. Brinkmeyer, R. Theunissen, P. M. Weaver, and A. Pirrera, "Adaptive compliant structures for flow regulation," *Proceedings of the Royal Society A: Mathematical, Physical and Engineering Sciences*, vol. 473, no. 2204, p. 20170334, 2017.

[16] E. Wheatcroft, J. Shen, R. M. J. Groh, A. Pirrera, and M. Schenk, "Structural function from sequential, interacting elastic instabilities," *Proceedings of the Royal Society A*, vol. 479, no. 2272, p. 20220861, 2023.

[17] N. An, A. G. Domel, J. Zhou, A. Rafsanjani, and K. Bertoldi, "Programmable hierarchical kirigami," *Advanced Functional Materials*, vol. 30, no. 6, p. 1906711, 2020.

[18] J. Shen, A. Pirrera, and R. M. J. Groh, "Building blocks that govern spontaneous and programmed pattern formation in pre-compressed bilayers," *Proceedings of the Royal Society A*, vol. 478, no. 2265, p. 20220173, 2022.

[19] B. Li, Y.-P. Cao, X.-Q. Feng, and H. Gao, "Mechanics of morphological instabilities and surface wrinkling in soft materials: a review," *Soft Matter*, vol. 8, no. 21, pp. 5728–5745, 2012.

[20] C.-M. Chen and S. Yang, "Wrinkling instabilities in polymer films and their applications," *Polymer International*, vol. 61, no. 7, pp. 1041–1047, 2012.

[21] T. Jin, X. Cheng, S. Xu, Y. Lai, and Y. Zhang, "Deep learning aided inverse design of the buckling-guided assembly for 3d frame structures," *Journal of the Mechanics and Physics of Solids*, vol. 179, p. 105398, 2023.

[22] Y. Tang, Y. Chi, J. Sun, T.-H. Huang, O. H. Maghsoudi, A. Spence, J. Zhao, H. Su, and J. Yin, "Leveraging elastic instabilities for amplified performance: Spine-inspired high-speed and high-force soft robots," *Science Advances*, vol. 6, no. 19, p. eaaz6912, 2020.

[23] A. Pal, V. Restrepo, D. Goswami, and R. V. Martinez, "Exploiting mechanical instabilities in soft robotics: control, sensing, and actuation," *Advanced Materials*, vol. 33, no. 19, p. 2006939, 2021.

[24] Y. Chi, Y. Li, Y. Zhao, Y. Hong, Y. Tang, and J. Yin, "Bistable and multistable actuators for soft robots: Structures, materials, and functionalities," *Advanced Materials*, vol. 34, no. 19, p. 2110384, 2022.

[25] J. Shen, M. Garrad, Q. Zhang, V. Wong, A. Pirrera, and R. M. J. Groh, "A rapid-response soft end effector inspired by the hummingbird beak," *Journal of the Royal Society Interface*, 2024. (Under review).

[26] K. Bertoldi, V. Vitelli, J. Christensen, and M. Van Hecke, "Flexible mechanical metamaterials," *Nature Reviews Materials*, vol. 2, no. 11, pp. 1–11, 2017.

[27] J. Bunyan and S. Tawfick, "Exploiting structural instability to design architected materials having essentially nonlinear stiffness," *Advanced Engineering Materials*, vol. 21, no. 2, p. 1800791, 2019.

[28] B. Deng, A. Zareei, X. Ding, J. C. Weaver, C. H. Rycroft, and K. Bertoldi, "Inverse design of mechanical metamaterials with target nonlinear response via a neural accelerated evolution strategy," *Advanced Materials*, vol. 34, no. 41, p. 2206238, 2022.

[29] J. Shen, M. Garrad, Q. Zhang, O. Leao, A. Pirrera, and R. M. J. Groh, "Active reconfiguration of multistable metamaterials for linear locomotion," *Physical Review B*, vol. 107, no. 21, p. 214103, 2023.
[30] J. M. T. Thompson, J. W. Hutchinson, and J. Sieber, "Probing shells against buckling: a nondestructive technique for laboratory testing," *International Journal of Bifurcation and Chaos*, vol. 27, no. 14, p. 1730048, 2017.
[31] R. M. Neville, R. M. Groh, A. Pirrera, and M. Schenk, "Beyond the fold: experimentally traversing limit points in nonlinear structures," *Proceedings of the Royal Society A*, vol. 476, no. 2233, p. 20190576, 2020.
[32] J. Shen, R. M. J. Groh, M. Schenk, and A. Pirrera, "Experimental path-following of equilibria using Newton's method. Part I: Theory, modelling, experiments," *International Journal of Solids and Structures*, vol. 210, pp. 203–223, 2021.
[33] J. Shen, R. M. J. Groh, M. Schenk, and A. Pirrera, "Experimental path-following of equilibria using Newton's method. Part II: Applications and outlook," *International Journal of Solids and Structures*, vol. 213, pp. 25–40, 2021.
[34] J. Shen, R. M. Groh, M. A. Wadee, M. Schenk, and A. Pirrera, "Probing the stability landscape of prestressed stayed columns susceptible to mode interaction," *Engineering Structures*, vol. 251, p. 113465, 2022.
[35] J. Shen, L. Lapira, M. A. Wadee, L. Gardner, A. Pirrera, and R. M. Groh, "Probing in situ capacities of prestressed stayed columns: towards a novel structural health monitoring technique," *Philosophical Transactions of the Royal Society A*, vol. 381, no. 2244, p. 20220033, 2023.
[36] R. M. J. Groh, D. Avitabile, and A. Pirrera, "Generalised path-following for well-behaved nonlinear structures," *Comput. Methods Appl. Mech. Eng.*, vol. 331, pp. 394–426, 2018.
[37] P. M. Reis, "A perspective on the revival of structural (in) stability with novel opportunities for function: from buckliphobia to buckliphilia," *Journal of Applied Mechanics*, vol. 82, no. 11, p. 111001, 2015.
[38] G. Wan, S. J. Avis, Z. Wang, X. Wang, H. Kusumaatmaja, and T. Zhang, "Finding transition state and minimum energy path of bistable elastic continua through energy landscape explorations," *Journal of the Mechanics and Physics of Solids*, vol. 183, p. 105503, 2024.
[39] A. Eriksson, "Structural instability analyses based on generalised path-following," *Computer Methods in Applied Mechanics and Engineering*, vol. 156, no. 1-4, pp. 45–74, 1998.
[40] J. Páez Chávez, Y. Liu, E. Pavlovskaia, and M. Wiercigroch, "Path-following analysis of the dynamical response of a piecewise-linear capsule system," *Communications in Nonlinear Science and Numerical Simulation*, vol. 37, pp. 102–114, 2016.
[41] R. M. J. Groh and A. Pirrera, "On the role of localizations in buckling of axially compressed cylinders," *Proceedings of the Royal Society A*, vol. 475, no. 2224, p. 20190006, 2019.
[42] F. Liu, X. Jiang, X. Wang, and L. Wang, "Machine learning-based design and optimization of curved beams for multistable structures and metamaterials," *Extreme Mechanics Letters*, vol. 41, p. 101002, 2020.
[43] G. Oliveri and J. T. Overvelde, "Inverse design of mechanical metamaterials that undergo buckling," *Advanced Functional Materials*, vol. 30, no. 12, p. 1909033, 2020.
[44] W. Li, F. Wang, O. Sigmund, and X. S. Zhang, "Digital synthesis of free-form multimaterial structures for realization of arbitrary programmed mechanical responses," *Proceedings of the National Academy of Sciences*, vol. 119, no. 10, p. e2120563119, 2022.
[45] X. Sun, K. Zhou, F. Demoly, R. R. Zhao, and H. J. Qi, "Perspective: Machine learning in design for 3D/4D printing," *Journal of Applied Mechanics*, pp. 1–30, 10 2023.
[46] A. Rafsanjani, A. Akbarzadeh, and D. Pasini, "Snapping mechanical metamaterials under tension," *Advanced Materials*, vol. 27, no. 39, pp. 5931–5935, 2015.
[47] C. Findeisen, J. Hohe, M. Kadic, and P. Gumbsch, "Characteristics of mechanical metamaterials based on buckling elements," *Journal of the Mechanics and Physics of Solids*, vol. 102, pp. 151–164, 2017.
[48] H. Yang, N. D'Ambrosio, P. Liu, D. Pasini, and L. Ma, "Shape memory mechanical metamaterials," *Materials Today*, vol. 66, pp. 36–49, 2023.
[49] S. Sun, N. An, G. Wang, M. Li, and J. Zhou, "Achieving selective snapping-back and enhanced hysteresis in soft mechanical metamaterials via fiber reinforcement," *Journal of Applied Physics*, vol. 129, no. 4, 2021.
[50] Y. Yan, J. Páez Chávez, J. Shen, and Y. Liu, "Dynamics of the vibro-impact capsule system with a von mises spring," *Nonlinear Dynamics*, 2024. Under review.
[51] J. Zhang, J. Tian, D. Zhu, Y. Liu, and S. Prasad, "Design and experimental investigation of a vibro-impact self-propelled capsule robot with orientation control," in *2022 IEEE International Conference on Robotics and Automation (ICRA)*, (Philadelphia, USA), pp. 11381–11387, 2022.
[52] J. Zhang, Y. Liu, D. Zhu, S. Prasad, and C. Liu, "Simulation and experimental studies of a vibro-impact capsule system driven by an external magnetic field," *Nonlinear Dynamics*, vol. 109, pp. 1501–1516, 2022.
[53] Y. Chi, Y. Hong, Y. Zhao, Y. Li, and J. Yin, "Snapping for high-speed and high-efficient butterfly stroke–like soft swimmer," *Science Advances*, vol. 8, no. 46, p. eadd3788, 2022.
[54] F. O. Falope, M. Pelliciari, L. Lanzoni, and A. M. Tarantino, "Snap-through and eulerian buckling of the bi-stable von mises truss in nonlinear elasticity: A theoretical, numerical and experimental investigation," *International Journal of Non-Linear Mechanics*, vol. 134, p. 103739, 2021.
[55] R. Masana, A. S. Dalaq, S. Khazaaleh, and M. Daqaq, "The kresling origami spring: A review and assessment," *Smart Materials and Structures*, 2024. (Accepted).
[56] J. Tian, K. O. Afebu, Z. Wang, Y. Liu, and S. Prasad, "Dynamic analysis of a soft capsule robot self-propelling in the small intestine via finite element method," *Nonlinear Dynamics*, vol. 111, no. 11, pp. 9777–9798, 2023.
[57] J. Qi, Z. Chen, P. Jiang, W. Hu, Y. Wang, Z. Zhao, X. Cao, S. Zhang, R. Tao, Y. Li, *et al.*, "Recent progress in active mechanical metamaterials and construction principles," *Advanced Science*, vol. 9, no. 1, p. 2102662,

2022.
[58] M. Sitti, "Physical intelligence as a new paradigm," *Extreme Mechanics Letters*, vol. 46, p. 101340, 2021.

Supplementary Materials for 'Enhancing the mobility of small-scale robots via nonlinear structural springs exhibiting negative stiffness'

1 Nonlinear mechanics of the *von Mises* truss and performance-based inverse design

Fig. S1(a) presents a *von Mises* truss connected in series with linear springs. This structure features an arch-like arrangement of two inclined linear springs k_1, a horizontal spring k_2 connecting two base nodes and a vertical spring k_3 connecting the actuation point and the apex. The rise of the truss is H and the span is L. Note that when the horizontal spring k_2 approximates to infinity, the truss will be identical to the classical *von Mises* truss discussed in authors' previous work [1]. A displacement controlled loading u_a is applied at the top of the vertical spring point. In this section, we will first present the analytical model for the *von Mises* truss and explore their design space. Subsequently, we introduce the performance-based inverse design framework, which seamlessly integrates the analytical model and the Generic Optimization algorithm. This inverse design tool will be used in the subsequent section for the parametric study on the propelling performance of the capsule robot.

1.1 Analytical model of the *von Mises* truss

Considering the simplicity of the structure, we can derive the governing equation for the equilibrium condition based on the direct equilibrium condition regarding the apex of the truss C, as shown in Fig. S1(b). For simplicity, we choose the vertical displacement at the apex u_apx as the primary variable:

$$F_\mathrm{a} = \frac{2k_1\left(H-u_\mathrm{apx}\right)\left(\sqrt{H^2+L^2/4}-\eta_1\right)}{\eta_1}, \tag{1}$$

where:

$$\eta_1 = \sqrt{\left[\frac{L}{2}-\frac{F_\mathrm{a}L}{2F_\mathrm{a}-8k_2\left(H-u_\mathrm{apx}\right)}\right]^2+\left(H-u_\mathrm{apx}\right)^2} \tag{2}$$

Note that the governing equation is implicit and is solved numerically using the embedded nonlinear solver in MATLAB. The actuation displacement at the actuation point can be expressed as follows:

$$u_\mathrm{a} = u_\mathrm{apx} + F_\mathrm{a}/k_3. \tag{3}$$

Note that if k_2 approximates infinity, the governing equation for the equilibrium is explicit and can be written as:

$$F_\mathrm{a} = 2k_1\left(H-u_\mathrm{apx}\right)\left(\frac{\sqrt{H^2+L^2/4}}{\sqrt{L^2/4+\left(H-u_\mathrm{apx}\right)^2}}-1\right) \tag{4}$$

Due to its simplicity, we utilise this extreme case for the integration with the capsule robot. However, in this section, we will continue to investigate the impact of k_2 on the nonlinear response of the *von Mises* truss.

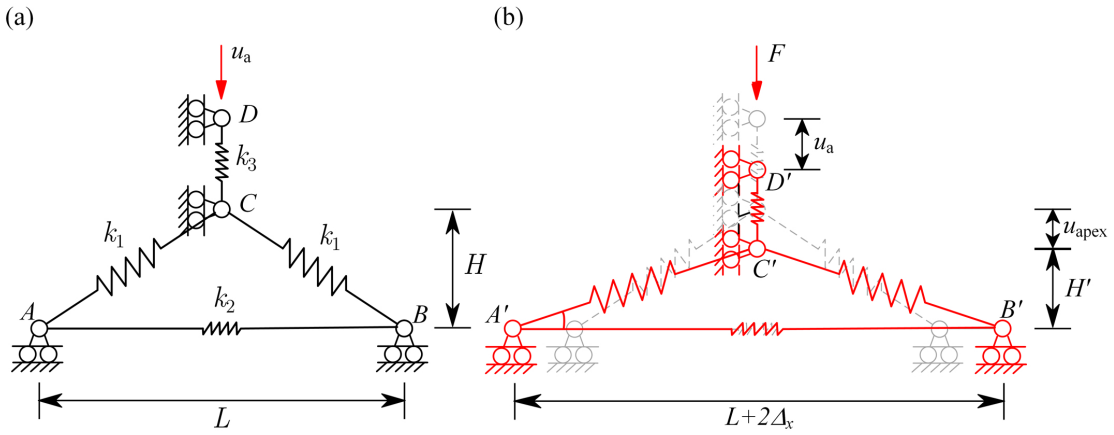

Figure S1: (a) *von-Mises* truss under displacement-contrlled loading at the apex. The stiffness is comprised of axial springs with stiffness k_1, k_2 and k_3. The span and rise of the truss is L and H, respectively. (b) Deformed state of the *von-Mises* truss under the actuation displacement at the apex.

1.2 Nonlinear behaviour of the *von Mises* truss

In this section, we will study how stiffness properties and rise–span ratio affect the behaviour of *von Mises* truss and their energy-release performance, which may potentially be converted into kinematic effects to enhance the speed, by exploiting the snap-down instability. We aim to address the following research questions: 1) the threshold condition for *von Mises* truss exhibiting snap-backs such that it can be used for energy release under displacement controlled loading; 2) how geometry properties and stiffness properties affects the energy transformation efficiency, scant stiffness, and ultimate load-carrying capacity of *von Mises* trusses.

To ensure that the *von Mises* truss effectively release energy through cyclic displacement controlled loading and unloading, it is crucial for the corresponding nonlinear equilibrium path to exhibit snap-back behavior, characterized by a pair of limit points. Fig. S2 illustrates three characteristic equilibrium paths of *von Mises* trusses: a) no displacement limit point; b) a single stationary point; c) a pair of limit points. Due to the structure's symmetry, the nonlinear equilibrium path intersects with horizontal axis ($F_a = 0$) at $u_a = 0,\ H,\ 2H$. When the pair of displacement limit points merge, *i.e.* the cusp of the fold line [2], it corresponds to the case in Fig. S2(b), which can be written as:

$$\left.\frac{\mathrm{d}u_a}{\mathrm{d}F_a}\right|_{u_a=H} = 0. \tag{5}$$

By substituting Eqs. (1) and (3) into Eq. (5), we can obtain the critical condition for *von Mises* truss exhibiting snap-backs:

$$\frac{4 + 2k_3/k_1}{4 - k_3/k_2} \leq \sqrt{4(H/L)^2 + 1}. \tag{6}$$

All the analysis conducted in the following subsections will be in the parameter space satisfying the constraint above. For illustration purposes, the corresponding phase change diagram for the case with $k_2 = \infty$ is presented in Fig. S3.

Moreover, a sensitivity study regarding the stiffness of the spring k_2 is conducted to determine the 'threshold' stiffness when these springs can be treated as rigid body. Instead of assessing the entire equilibrium path, we select the maximum load-carrying capacity as the index, *i.e.* $\mathrm{d}F/\mathrm{d}u_a = 0$:

$$F_{\max} = \frac{2k_1k_2L}{k_1 + 2k_2}\eta_2^3, \tag{7}$$

where $\eta_2 = \sqrt{\left[4(H/L)^2 + 1\right]^{\frac{1}{3}} - 1}$.

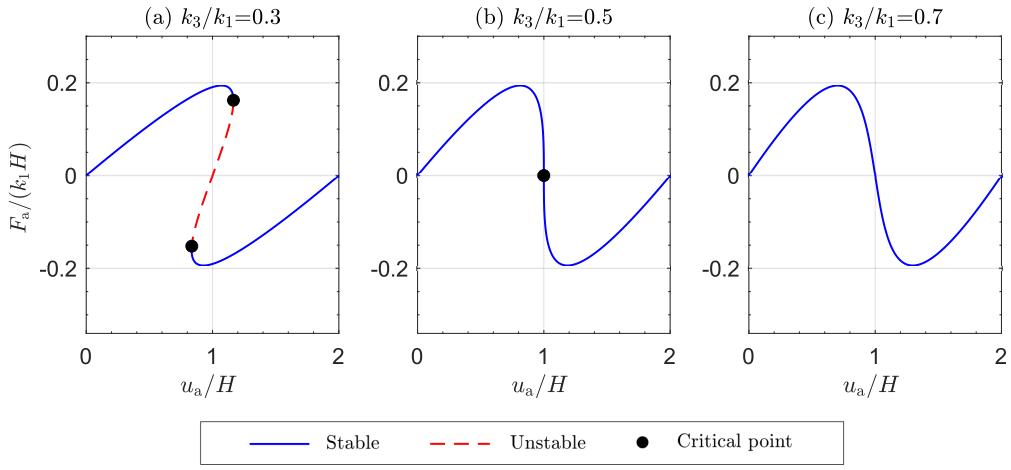

Figure S2: Three characteristic equilibrium paths of *von Mises* truss under displacement control loading: (a) with a pair of limit points; (b) with a single limit point; (c) without displacement limit point. Note that the geometry and material properties of the *von Mises* truss are: H=400 mm, L=1600 mm, k_1=20 N/mm, k_2=100 N/mm.

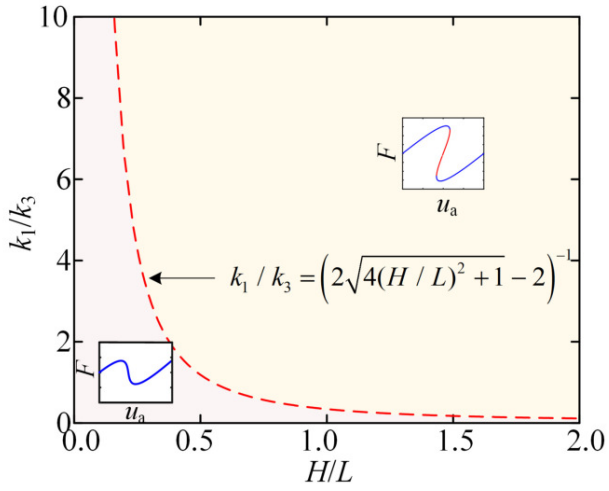

Figure S3: Phase change diagram for the *von Mises* truss with $k_2 = \infty$. The dashed curve represent the fold line where the limit points for displacement-controlled loading merge, *i.e.* the boundary where the *von Mises* truss exhibits snap-back.

The sensitivity of $F_{\max}$ to k_2 can be determined by solving the partial derivatives of $F_{\max}$ regarding to k_2:

$$\frac{\mathrm{d}F_{\max}}{\mathrm{d}k_2} = \frac{2k_1^2 L\eta_2^3}{(1+2k_2)^2} \tag{8}$$

When $k_2/k_1 = 9.5$, $F_{\max}/F_{\max,k_2/k_1\to\infty} = 0.95$; $k_2/k_1 = 49.5$, $F_{\max}/F_{\max,k_2/k_1\to\infty} = 0.99$. Further increase in k_2/k_1 only leads to an infinitesimal increase in $F_{\max}/F_{\max,k_2/k_1\to\infty}$. For economical design, we assume that the horizontal spring can be treated as a rigid bar for cases $F_{\max}/F_{\max,k_2/k_1\to\infty} > 0.99$.

1.3 Key performance indexes and sensitivity study

Considering that the *von Mises* truss functions as a load-carrying component within the capsule robot, we define the initial tangent stiffness k_{ini} maximum load $P_{\max}$ and the corresponding scant stiffness k_{scant} at

Table S1: Geometry and stiffness properties of the baseline *von Mises* truss.

L (mm)	H (mm)	k_1 (N/mm)	k_2 (N/mm)	k_3 (N/mm)
600	400	20	40	10

$P_{\max}$ as the key performance indexes, as illustrated in Fig. S4. These indexes provide valuable insights into the truss's structural behavior and energy dissipation performance under loading conditions. A MATLAB script is specifically developed for computing these indexes based on a specific set of parameters.

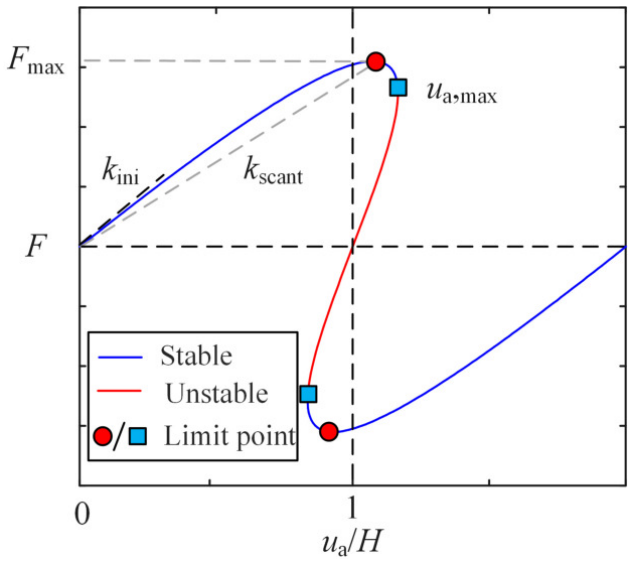

Figure S4: Illustration of the key performance indexes of the *von Mises* truss.

To understand how the design parameters affects these performance index, a sensitivity study is conducted. Fig. S5 presents the sensitivity of the nonlinear equilibrium path and the key performance indexes of *von Mises* truss to the spring stiffness and the span L. The energy dissipated and the displacement to trigger the snap-down instability $u_{a,\max}$ increases with the increasing k_1. For the scant stiffness, it initially increases and then reaches a plateau. Note that there is a lower boundary for k_1, below which the equilibrium path exhibits no snap-back and consequently, zero energy dissipation occurs. The corresponding lower bound can be determined using Eq. (6).

Similar to k_1, increasing the parameter k_2 also results in the improvement of the three performance indexes, as shown in Fig. S5(b). This is in accordance with the previous study on 3D latticed structured materials [3]. However, unlike the behavior observed for k_1, we observe a plateau in the energy dissipation $\bar{E}_{\text{disp}}$ and $\bar{u}_{a,\max}$ as k_2 surpasses a certain threshold stiffness. Beyond this point, further increases in k_2 yield only marginal improvements in the performance indexes. The upper threshold can be determined using Eq. (8) based on the specific requirement. There is also a lower bound for k_2, which can also be determined using Eq. (6).

Unlike k_1 and k_2, the increase of k_3 leads to the drop in the dissipated energy and $u_{a,\max}$ but increase in the scant stiffness. Accordingly, there is an upper threshold for k_3, which is determined by Eq. (6), above which the system will not dissipate energy during the cyclic loading. The increase of the span L leads to the drop in all three performance indexes. Similar to k_3, there is a upper limit for L, above which there will be no energy dissipation. The upper limit can also be solved using Eq. (6).

1.4 Performance-based inverse design of *von Mises* truss

The extensive parametric studies in the previous section thoroughly examined the nonlinear mechanics of the *von Mises* truss under varying geometry and stiffness properties. However, in practical applications

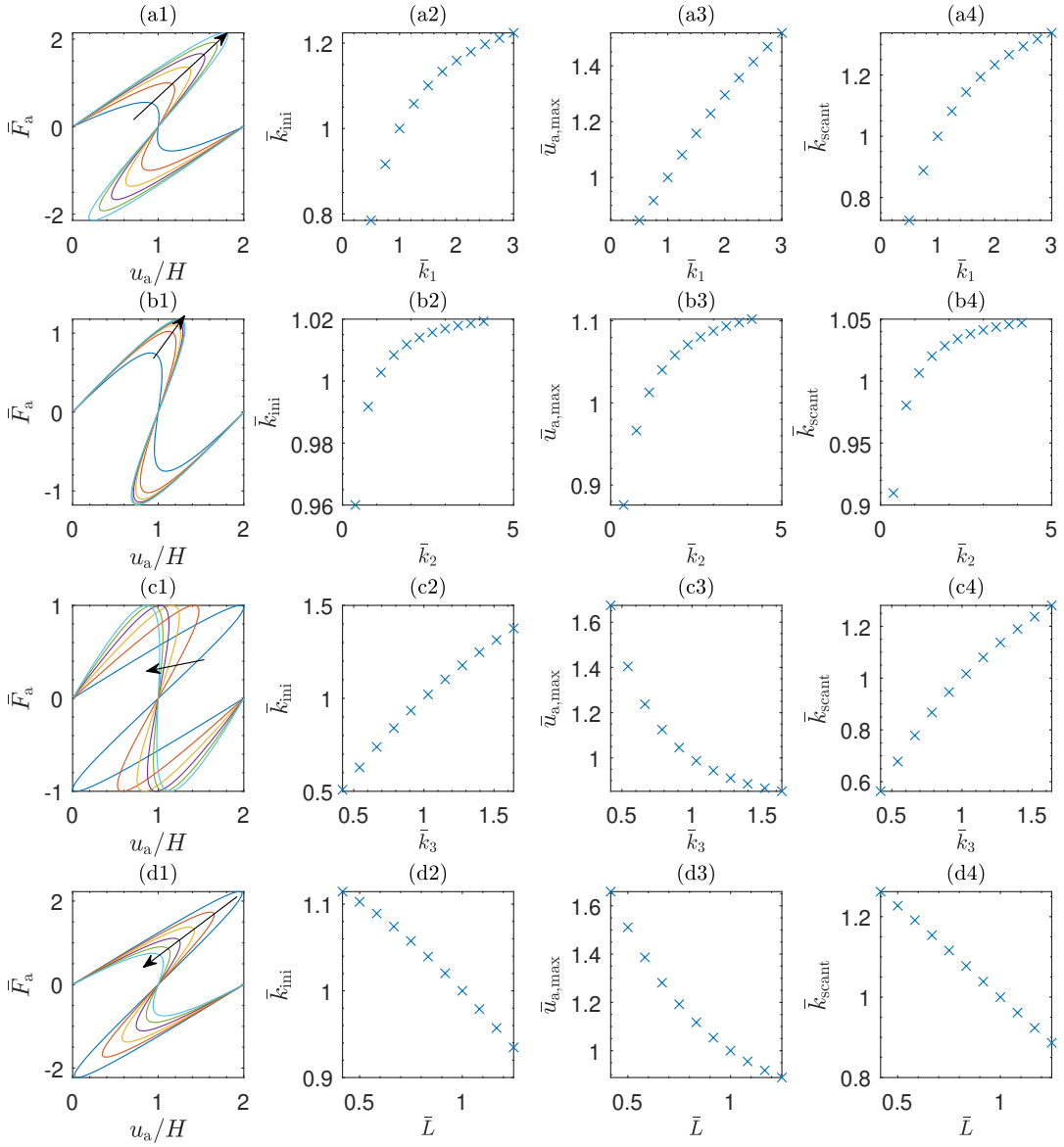

Figure S5: Sensitivity of key performance indexes of the *von Mises* truss to (a) the stiffness of inclined spring k_1, (b) the horizontal spring k_2, (c) the vertical spring k_3 and (d) the span L. All the quantities are normalised with respect to those of the baseline structure with the geometry and stiffness properties of the baseline *von Mises* truss presented in Table S1. The arrows in (1) represent the increasing of the varying design parameter.

for functionalised nonlinear structures, the inverse problem holds greater significance, where the goal is to determine the geometry and stiffness properties to achieve the desired performance. To address this inverse design problem, we formulate it as an optimization problem, where the objective function can be the entire equilibrium path or the targeted performance indexes, as illustrated in Fig. S4. Owing to the analytical equation derived for the nonlinear equilibrium path of the *von Mises* truss (Eq. (3)), the solution process is as efficient as those employing trained machine learning models [4, 5] while offering enhanced accuracy and robustness.

Here, to reduce the dimension of the problem and further improve the computational efficiency, we only select the key performance indexes as the objective function, rather than considering the entire nonlin-

ear equilibrium path as in previous studies [5]. This simplified approach proves adequate for the current study. The framework for the performance-based inverse design or optimisation is presented in Fig. S6. When employing the genetic algorithm (GA) for variable updating, critical parameters—such as population size, mutation rate, crossover rate, and maximum number of iterations—are set to 50, 0.05, 0.6, and 100, respectively.

The optimisation problem is formulated as:

$$\begin{aligned} \underset{\mathbf{x}}{\text{minimize}} \quad & \text{Loss} = \left(Y - \widetilde{Y}\right)^2 \\ \text{subject to} \quad & m \leq m_{\text{baseline}} \\ & u_{\text{a,max}} \leq 2H \end{aligned} \tag{9}$$

where $\mathbf{x}$ are the design parameters of the *von Mises* truss listed in Table S1.

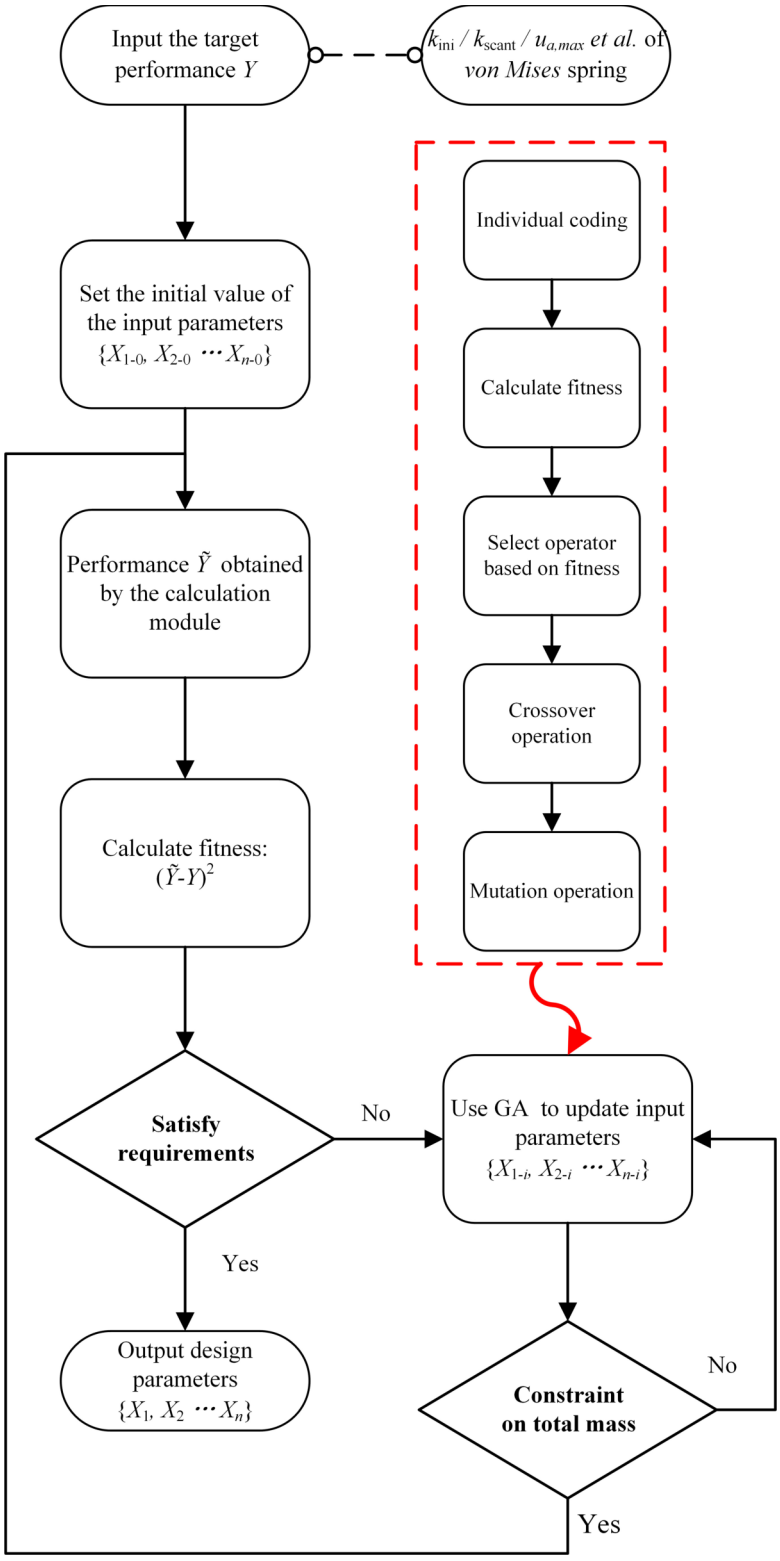

Figure S6: Flowchart for the performance-based inverse design of the *von Mises* truss spring.

2 Parametric study

In addition to the results presented in the main paper, we have conducted some more analysis to understand the mechanics of the capsule integrated with the *von Mises* truss. If not specified, the parameters adopted here are the same as that in the main paper, as presented in Table S2, which is the same as in the main paper.

Table S2: System and control parameters of the capsule robot.

Parameters	Unit	Values
Inner mass weight M_{m}	g	1.8
Capsule weight M_{c}	g	1.67
Friction factor μ	–	0.59
Vertical spring of *von Mises* truss k_1	kN/m	[0,0.1]
Inclined spring of *von Mises* truss k_3	kN/m	0.062
Rise of the *von Mises* truss H	mm	[0.8,0.9]
Span of the *von Mises* truss L	mm	[1,1.5]
Forward constraint spring k_{f}	kN/m	53.5
Backward constraint spring k_{b}	kN/m	27.9
Magnitude of the excitation force P_{d}	mN	$[10, 80]$
Frequency of the excitation Ω	Hz	$[1, 50]$

2.1 *von Mises* truss with $k_1 = \infty$

In order to understand the effects of spring stiffness and the net distance on the dynamic response of capsule robot, we first investigate the scenario with a linear spring, *i.e.* $k_1 = \infty$. Fig. S7 illustrates the average speed of the capsule robot in the parameter space defined by $k_{\mathrm{s}} = [0,\ 0.1]$ kN/m and $G_1 = [0.2,\ 1.0]$ mm. In this parameter range, the propelling speed reaches its maximum at $k_{\mathrm{s}} = 0.025$ kN/m and $G_1 = 0.5$ mm. The average speed exhibits a highly nonlinear relationship with G_1 and k_{s}. For capsule robots with $G_1 > 0.7$ mm, the highest average speed occurs at $k_{\mathrm{s}} = 0$ kN/m, decreasing as k_{s} increases. With a further increase in k_{s}, the average speed becomes negative, indicating backward motion. The magnitude of average velocity then decreases. For cases with G_1 =0.4–0.6 mm, the average speed increases with k_{s} initially. A subsequent increase in k_{s} leads to a drop in velocity, followed by an increase and, finally, a decrease to zero. We also plot a red curve defining $G_1 k_{\mathrm{s}} = F_{\mathrm{e}}$ for reference. Under the quasi-static case, the inner mass would not collide with the capsule. Here, above the curve, the average speed of the capsule is almost zero.

Fig. S7(b–d) and (e–g) depict the time history of capsules with initial net gaps of $G_1 = 0.8$ mm and 0.5 mm, respectively. For each case, three characteristic capsule responses are presented, corresponding to forward movement with the highest average speed, forward movement with almost zero average speed, and backward movement. In the scenario with the highest forwarding speed, the relative speed of the inner mass increases as it approaches the rigid constraint spring, as illustrated in Fig. S7(b) and (f), resulting in a larger momentum transfer to the capsule. Moreover, the relative velocity during backward movement collides with the constraint spring with less velocity than during forward movement.

2.2 Results for *von Mises* truss with $k_3 = \infty$

In the main paper, we only present the results for the case with a fixed excitation force amplitude. Here, we present their sensitivity to the excitation force amplitude. The results are presented in Fig. S8. The parametric analysis is based on the results of the linear spring system. We select the case with the largest average speed, *i.e.* $G_1 = 0.5$ mm and $k_{\mathrm{s}} = 0.025$ kN/m as the reference baseline state. In all the subsequent analysis, we set $G_1 = 0.5$ mm and the scant stiffness at the force limit point, see Fig. S4, is identical to the stiffness of the linear spring, *i.e.* $k_{\mathrm{scant}} = 0.025$ kN/m. We adopt the performance inverse design tool developed in Section 1.4 to back-calculate the stiffness and the geometry of the *von Mises* truss to ensure that the initial tangent or scant stiffness of all the *von Mises* truss are identical.

We select four characteristic *von Mises* truss nonlinear springs in the parametric study, as shown in Fig. S8(a). They have the identical initial tangent stiffness, with different characteristic points locating at

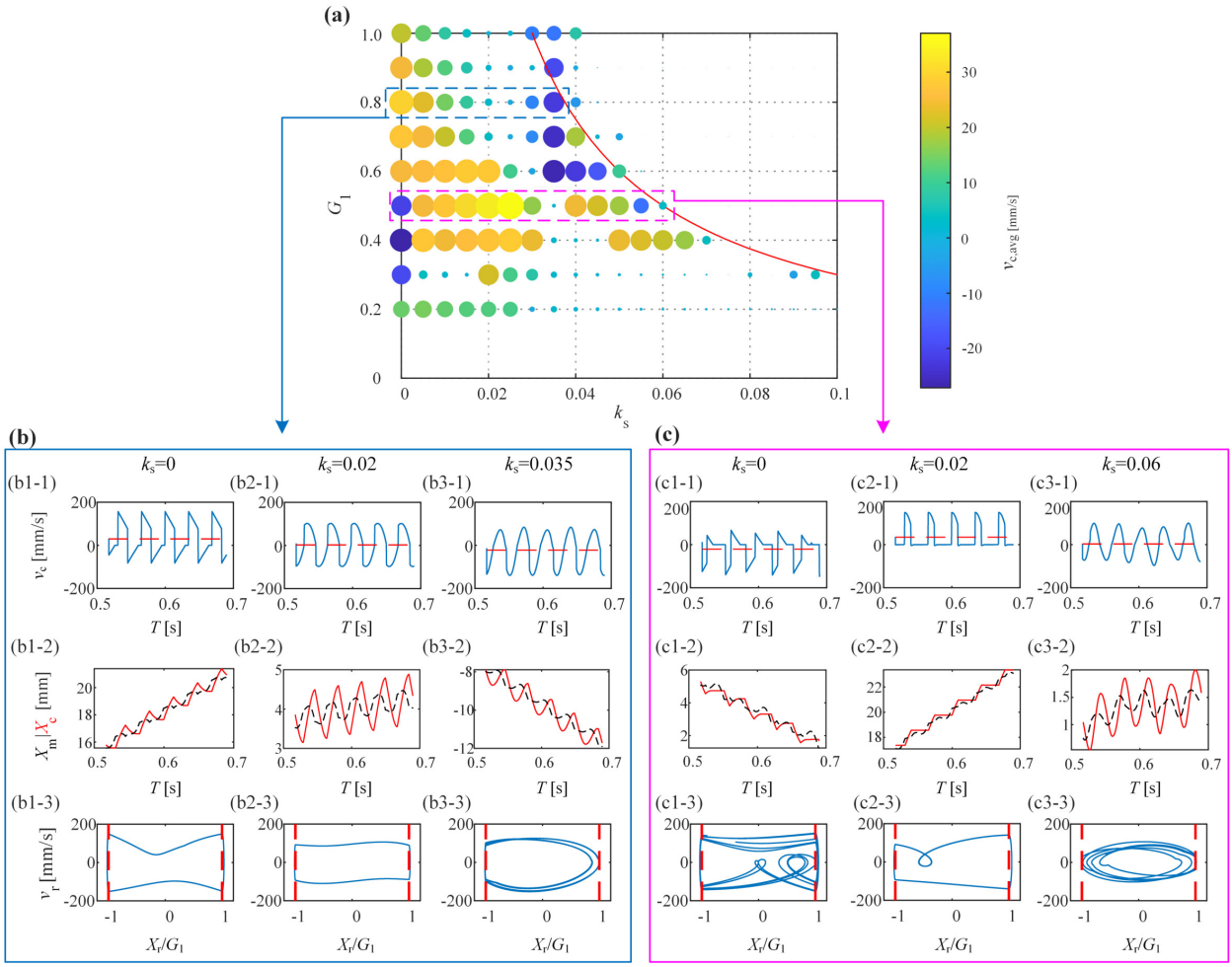

Figure S7: (a) Sensitivity of the average propelling velocity of the capsule robot to linear spring stiffness k_s and the initial gap distance G_1. Subfigures (b) and (c) show the time history results for the capsule with different linear spring stiffness for $G_1 = 0.8$ mm and $G_1 = 0.5$ mm, respectively. The first row shows the propelling speed (blue curve) as well as the average speed (red dashed line) versus time; the second row shows the displacement history of the inner mass and the capsule; the third row shows the normalised relative displacement of the inner mass x_r/G_1 versus the relative velocity v_r. The reference red dashed lines at $x_r/G_1 = \pm 1$ represent the inner mass colliding with the capsule.

$u_a = G_1$: case 1, the snap-through point with $F_a = F_{max}$ locates at $u_a = G_1$; in case 2, the local minimum with $F_a = -F_{max}$ locates at $u_a = G_1$; in case 3, the transitional unstable equilibrium with $F_a = 0$ locates at $u_a = G_1$; in case 4, the local maximum locates at $u_a = G_1$. Fig. S8(b–d) presents the average velocity of the capsule robot in the frequency range [0 50] Hz and different excitation force levels. When the excitation force is modest $P_d \leq 5$ mN, the average velocity for for all configurations is nearly zero. This is because the critical load of all the *von Mises* trusses in this situation is larger than the excitation force, preventing the interior mass from colliding with the capsule. Moreover, the corresponding reaction force applied on the capsule is smaller than the friction. With the increase of the excitation force P_d, the maximum average velocity for each configuration increases and then drops with further increase of P_d.

When the excitation force magnitude $P_d \geq 10$ mN, *i.e.* the critical load of all *von Mises* truss, the average velocity of the capsule robot exhibits sensitivity to the excitation frequency Ω. Generally, the average velocity is small for both extremely low and high frequency regimes. In the intermediate excitation frequency domain, there are dramatic changes in the both the magnitude and the sign of the average velocity. Compared with case 4, which exhibits no negative stiffness, the other three cases have a relatively large domain of high average

velocity. This implies that the system is relatively robust and their performance is less sensitive to noises and uncertainties. To gain insights into the mechanics, we present the time history results of the capsule robot with case 3 *von Mises* truss and the excitation force $P_\mathrm{d} = 10$ at selected excitation frequency in Fig. **??**. If the excitation frequencies are too low or high, the inner mass exhibits irregular chaotic responses, resulting in aperiodic capsule movements. Note that the transition regime where the average velocity changes sign also coincides with the chaotic response of the inner mass. The peak average forward velocity corresponds to a periodic response of the inner mass. The capsule with case 3 *von Mises* truss shows a larger domain of periodic inner mass response compared to that with the case 4 *von Mises* truss, as shown in Figs. S9 and S10.

Of all four cases under the excitation force $P_\mathrm{d} = 20$ mN, the capsule robot with case 3 *von Mises* truss exhibits the highest average propelling speed as well as the widest frequency domain to maintain a relatively high propelling speed. Thus, we conducted the sensitivity of the excitation force amplitude P_d on the highest propelling speed for the case 3 *von Mises* truss in the excitatino frequency domain [10 50] Hz. As shown in Fig. S11(a), the highest average speed of the capsule robot initially increases with the excitation forces, reaching the plateau about 20 mN. With the further increase of the excitation force, the peak average speed $v_{\mathrm{pro,avg}}$ drops. Note that the corresponding excitation frequency at the largest $v_{\mathrm{pro,avg}}$ for each case exhibits a similar trend, as shown in Fig. S11(b). Fig. S11(c) presents the phase portraits of the inner mass and the time history results for the displacement of both the capsule and inner mass for three characteristic cases. When the excitation force amplitude $P_\mathrm{d} = 12$ mN, the relative velocity of the inner mass remains small, causing it only collides with the front constraint spring. As P_d increases, the relative velocity of the inner mass escalates, bringing it closer to the back constraint spring. Simultaneously, the left half of the phase portrait transits from sharp to rounded profile, due to the stiffening effects of *von Mises* truss in the tension regime. The further increase in the excitation force leads to a drop in the largest $v_{\mathrm{pro,avg}}$. This arises from the chaotic response of the inner mass, as illustrated in Fig. S11(c3-1). The second and third rows of Fig. S11(c) present the time history results for the velocity and displacement of the inner mass and the capsule. For cases with $P_\mathrm{d} = 12$ mN and $P_\mathrm{d} = 18$ mN, the graph patterns are very similar to those with negative stiffness in Fig. 2(c) in the main paper, but with different velocities. For the case with $P_\mathrm{d} = 12$ mN, the capsule almost remains stationary before the first collision due to the fact that the reaction force applied on the capsule cannot overcome the friction. For the case with $P_\mathrm{d} = 40$ mN, the displacement per period (almost four times of that for $P_\mathrm{d} = 18$ mN) and the velocities of the inner mass and the capsule are much larger than the other two cases. However, as depicted by the velocity history (closely located abrupt jumps), there are multiple collisions between the inner mass and the capsule in a typical 'period'. This makes the effective velocity lower than those with periodic solutions and less energy efficient.

From the results, we could conclude that the negative stiffness of the *von Mises* truss make the overall capsule robot less sensitive to the excitation frequency. Since the *von Mises* truss exhibits nonlinearity before the critical point, the scant stiffness at the origin may not be representative enough, we also conducted a sensitivity study on cases with identical scant stiffness. The results are shown in Fig. S12. Note that they exhibit almost identical trend as those with identical tangent stiffness. Note that among all five cases, cases 2 and 3 exhibit a relative wide working frequency band with relatively high average propelling velocity. This is in accordance with our findings in the main paper. In case 1, the stiffening effects of the *von Mises* truss in proximity of $X_\mathrm{r} = G_1$ undermines the robustness of the capsule robot, making it sensitive to excitation frequency.

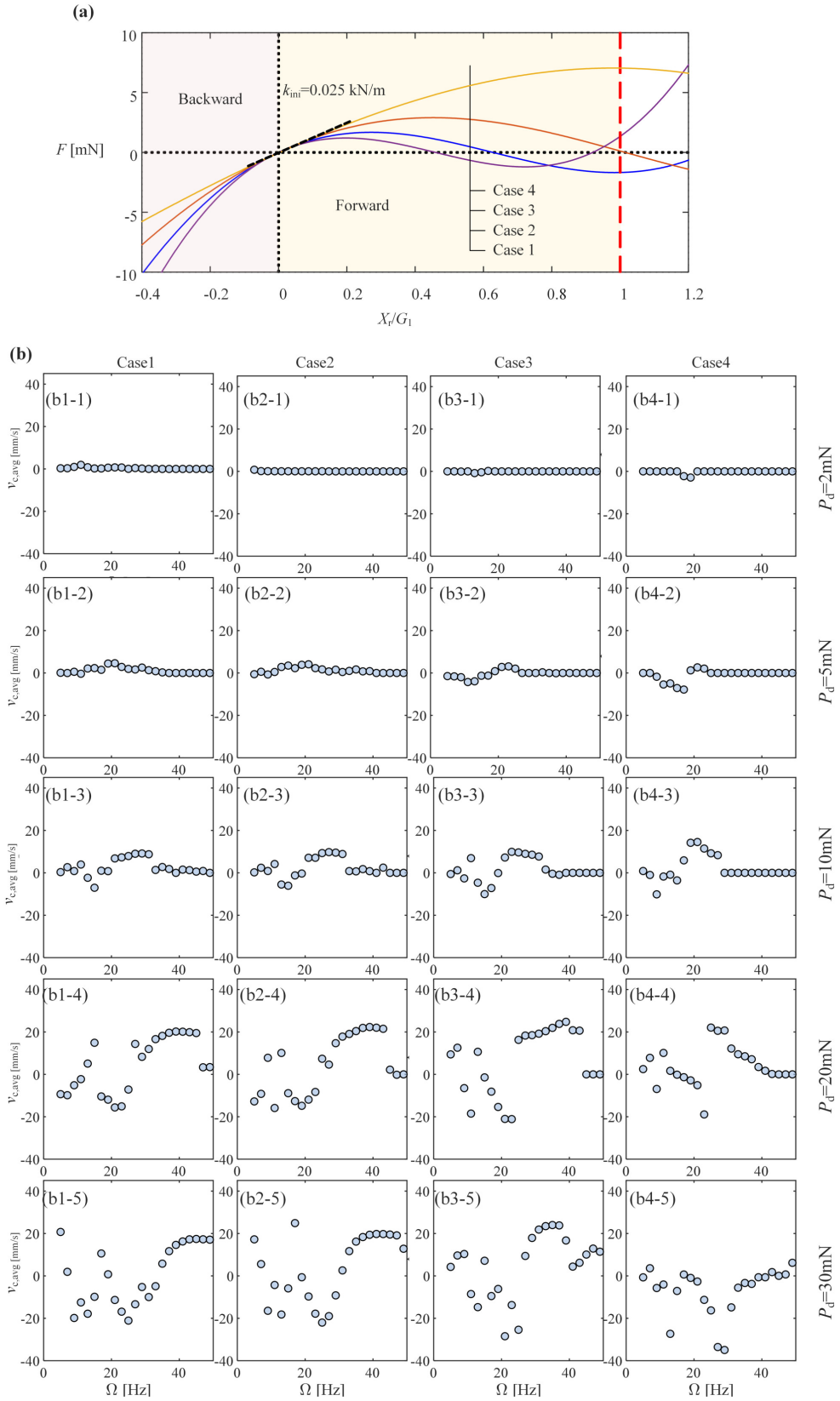

Figure S8: The average propelling speed of the capsule robots with the *von Mises* truss springs with identical initial stiffness but different rises and peak loads. (a) Nonlinear equilibrium paths of the three characteristic *von Mises* trusses. (b) Average propelling speed of the capsule robot at selected excitation force amplitude in the excitation frequency ranging from 10 to 50 Hz.

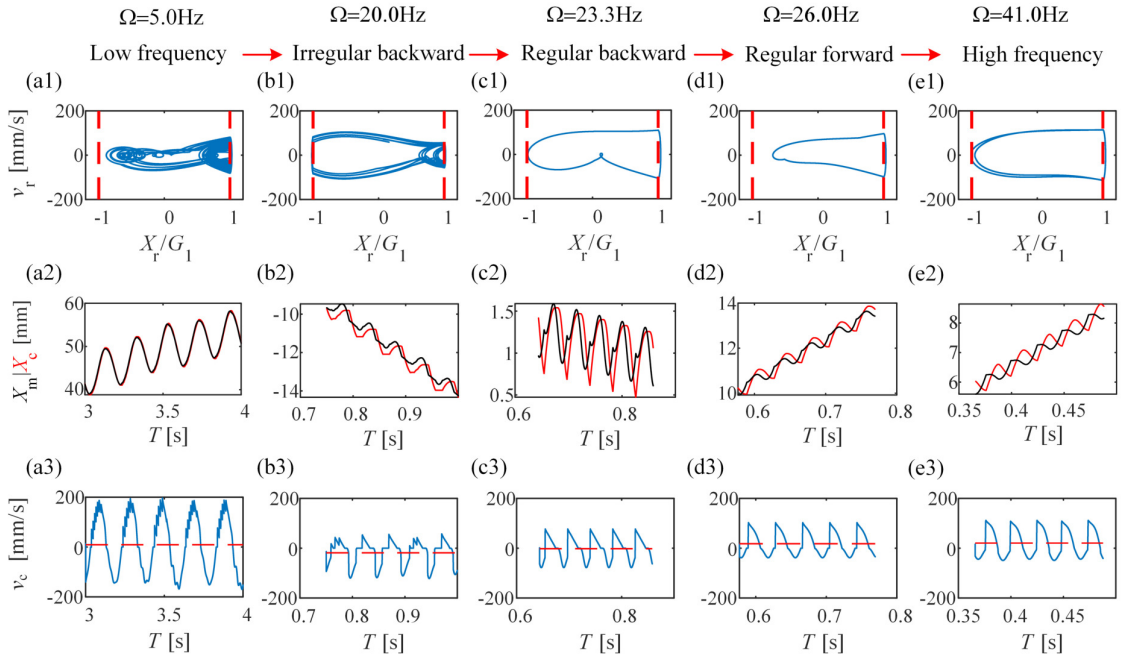

Figure S9: Time history of the capsule robots with the *von Mises* truss supporting springs corresponding to cases 3 in Fig. S8(a). Note that the excitation force amplitude $P_d = 20$ mN in all cases.

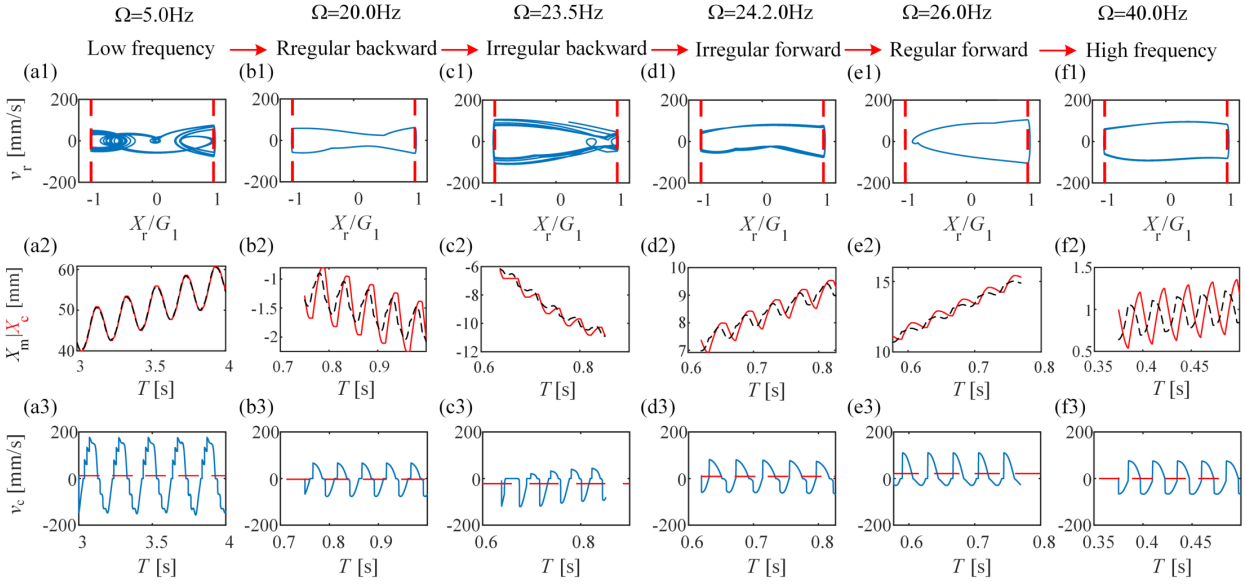

Figure S10: Time history of the capsule robots with the *von Mises* truss supporting springs corresponding to cases 4 in Fig. S8(a). Note that the excitation force amplitude $P_d = 20$ mN in all cases.

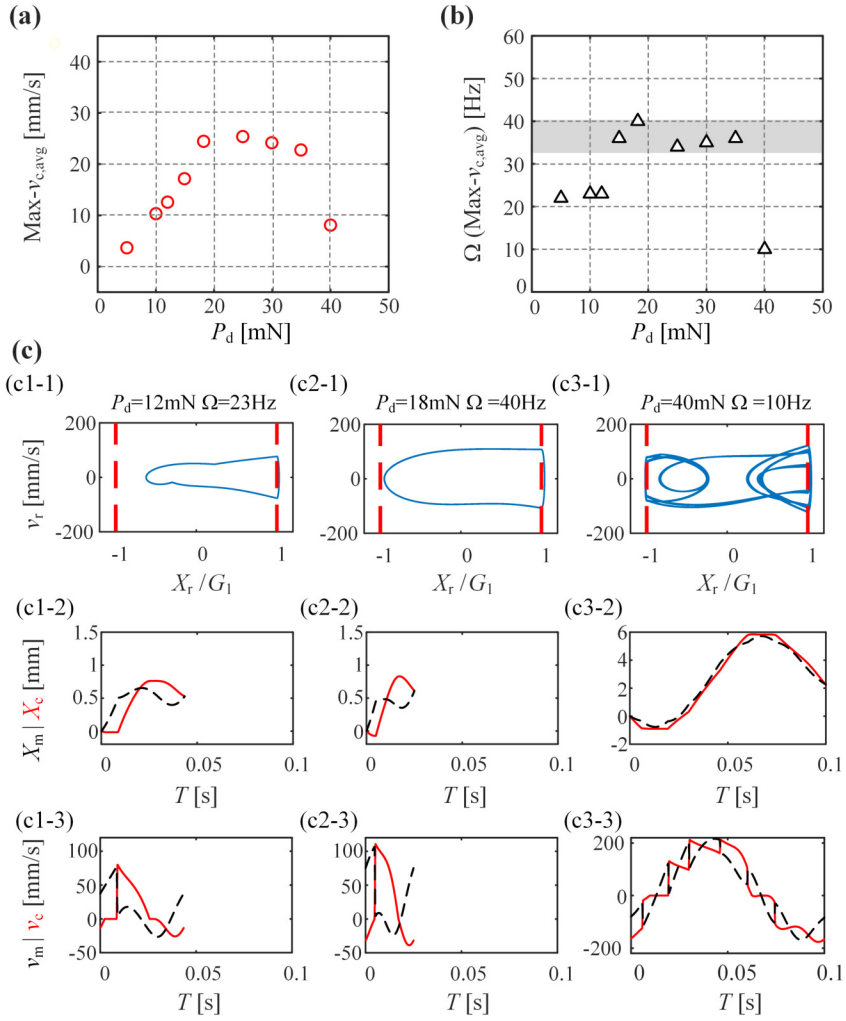

Figure S11: (a, b) The maximum propelling speed of the capsule robots with case 3 *von Mises* truss in Fig. S8(a) at excitation force amplitude ranging from 5 to 40 mN and the corresponding excitation frequency. (c) The phase portraits and time history results for the displacement of the inner mass and the capsule at selected excitation forces. (c) The phase portraits and time history results of the capsule robots exhibiting highest average propelling velocity in (b). First row presents the relative velocity of the inner mass at different positions in a period of excitation circle. The thick red dashed red lines represent the front and back constraint springs. The thin blue dashed lines represent the force limit point, *i.e.* the starting point of the negative stiffness. The second and third rows present the time history for the displacement and velocity of the capsule robot (red solid curve) and the inner mass (black dashed curve) for a single period.

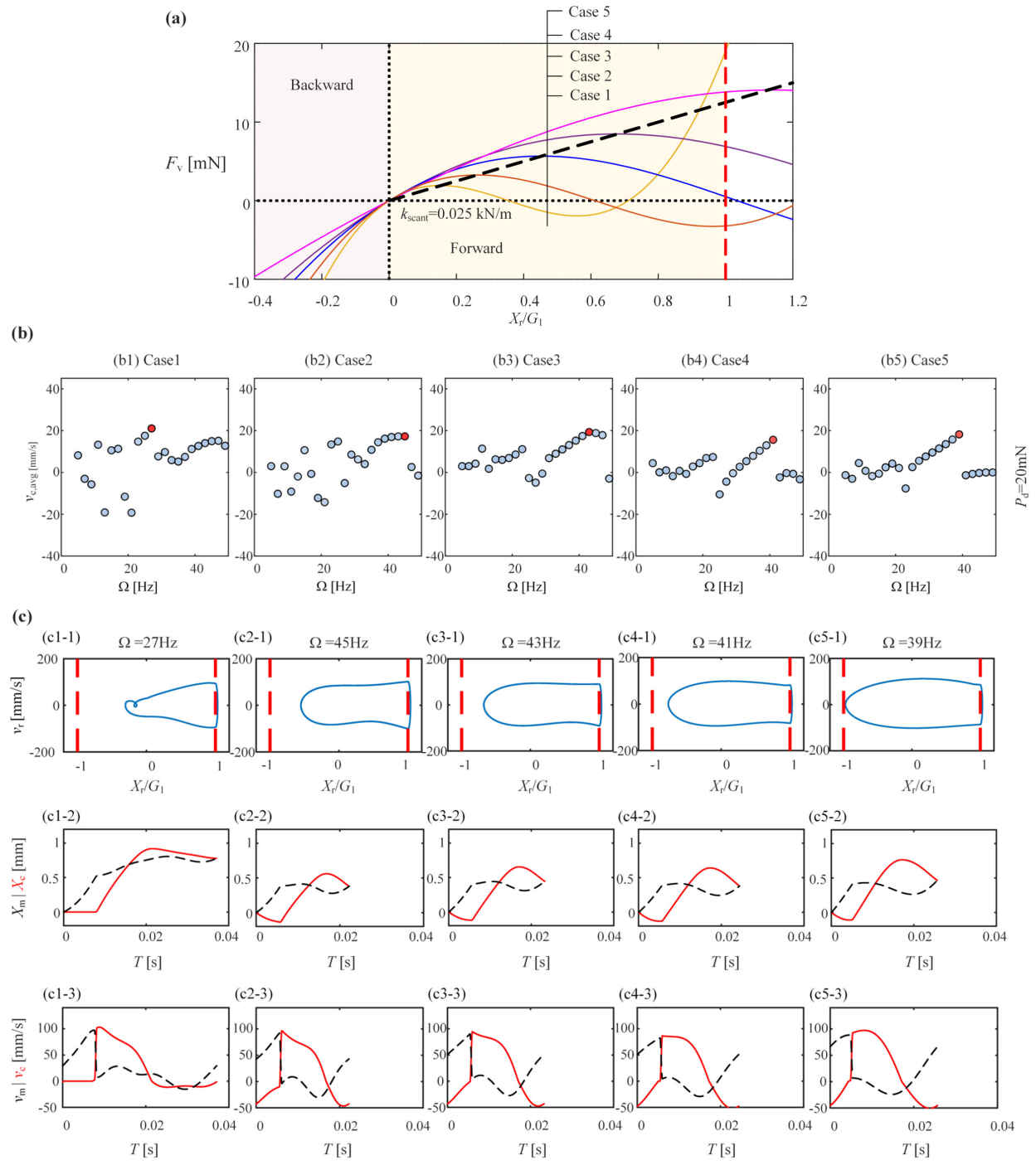

Figure S12: The average propelling speed of the capsule robots with the *von Mises* truss springs with identical secant stiffness but different rises and peak loads. (a) Nonlinear equilibrium paths of the three characteristic *von Mises* trusses. (b) Average propelling speed of the capsule at selected excitation force amplitude in the excitation frequency ranging from 10 to 50 Hz. (c) Phase portraits and time history results for the displacement and velocity of the inner mass and the capsule robots with the highest average speed for selected case in (b). The subfigures are as described in Fig. S11(c).

2.3 Effects of initial stiffness and snap-back on the nonlinear equilibrium path

In the main paper, we only present the results for the case with a single excitation force amplitude $P_{\mathrm{d}} = 20$ mN. Here, we present their sensitivity to P_{d}, as shown in Fig. S13. Similar to that in Fig. S8, the average speed of the capsule is almost zero when the excitation force is small, due to the fact that the reaction force applied on the capsule is lower than the friction force. At $P_{\mathrm{d}} = 30$ mN, cases 2 and 3 exhibit a relatively wide frequency band with high average propelling speed. However, upon closer inspection of the phase portraits and time history results, we find that their response is aperiodic, suggesting that the energy efficiency might not be as favorable as those exhibiting periodic responses, *i.e.* case 4.

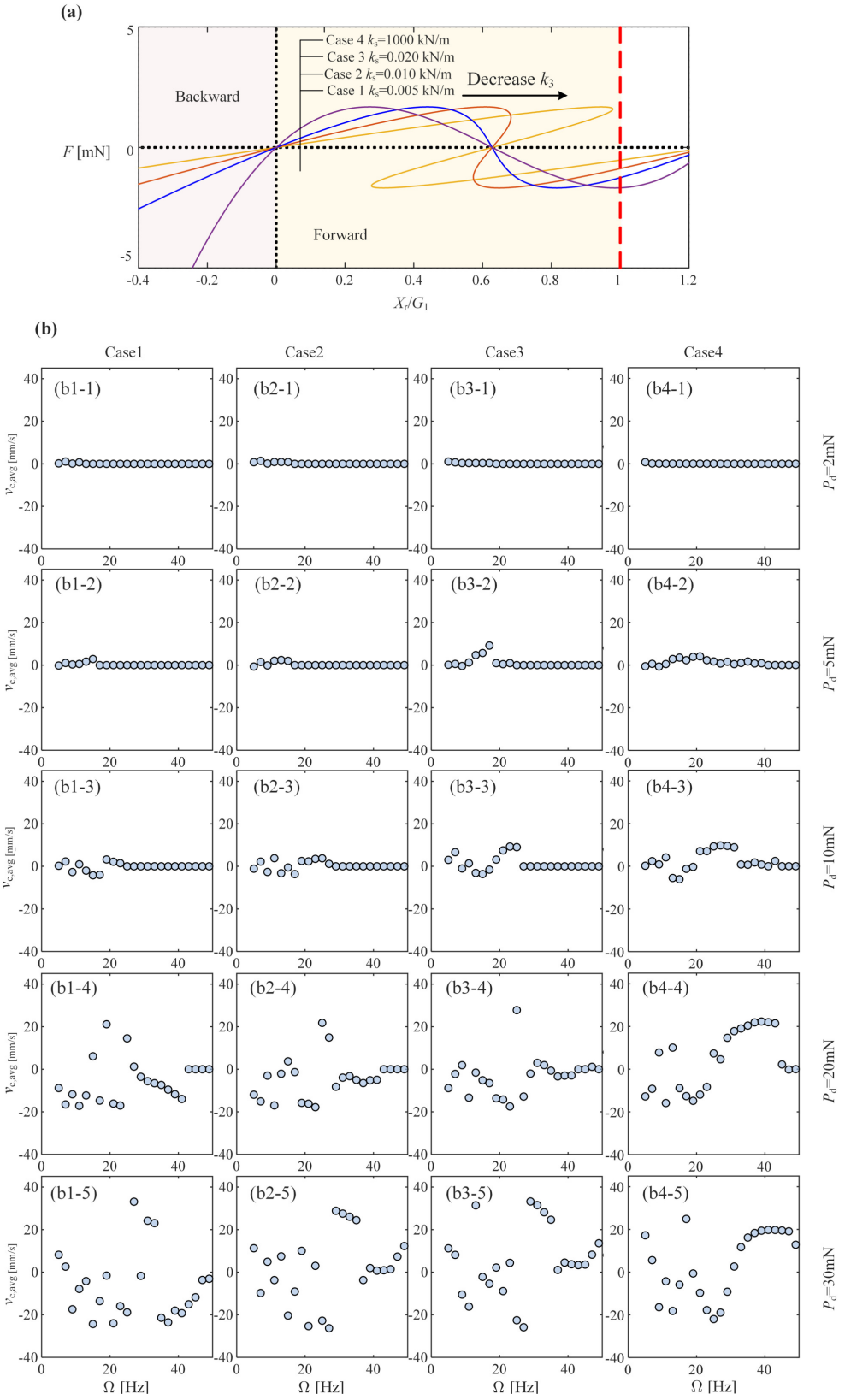

Figure S13: (a) The nonlinear equilibrium paths of the *von Mises* truss with different horizontal spring stiffness k_3. (b) Average propelling speed of the capsule robot at selected excitation force amplitude in the excitation frequency ranging from 10 to 50 Hz.

3 Optimisation of *von Mises* truss to boost the propelling performance of capsule robot

From the parametric studies in Section 4 of the main paper, we deduce that an optimally performing capsule robot should demonstrate a relatively high propelling speed over a broad excitation frequency range. This range is defined as the operational frequency band $\Delta\Omega_{\text{op}}$. This design choice can also ensure that the response of the inner mass and capsule remains periodic, ultimately leading to enhanced energy efficiency. In this section, we present an optimisation formulation to solve the geometry and stiffness properties of the *von Mises* truss that leads to an optimally performing capsule robot under the structural weight constraint of the *von Mises* truss. Here, we define the structural weight as the sum of the product of the stiffness of the component springs and their length.

Since the snap-back behaviour of the *von Mises* truss leads to a high sensitivity to excitation frequency, the optimisation only focuses on the case with a rigid horizontal spring, *i.e.* $k_3 = \infty$. Moreover, we set the case 3 *von Mises* in Fig. 2(a) in the main paper as the baseline, with its structural weight serving as a constraint in the optimization formulation. Mathematically, the optimisation formulation is stated as:

$$\begin{aligned} \underset{k_1,\ H,\ L}{\text{maximize}} \quad & v_{\text{max,avg}} \cdot \Delta\Omega_{\text{op}} \\ \text{subject to} \quad & m \leq m_{\text{baseline}} \end{aligned} \tag{10}$$

where $v_{\text{max,avg}}$ is the average speed of the capsule robot within a window characterized by high speed and a broad frequency band, as illustrated in Fig. S14(b); $m = k_1\sqrt{H^2 + L^2/4}$ is the structural weight of the *von Mises* truss (excluding k_3 as we assume that the horizontal spring is rigid and the force is directly applied to the apex).

As for the computation of the objective function, we begin by computing the average propelling velocity of the capsule robot at each excitation frequency within the domain [10 50] Hz and the excitation force amplitude $P_{\text{d}} = 20$ mN. From these data, we identify the maximum average velocity v_{max}. Then, we define an acceptable high propelling velocity range, which is expressed as $[\kappa v_{\text{max}},\ v_{\text{max}}]$. The average speed within this high velocity window is denoted as $v_{\text{max,avg}}$, and the corresponding frequency span of the velocity window is $\Delta\Omega_{\text{op}}$. Moreover, we include the constraint $\Delta\Omega_{\text{op}} \leq 5$ in the objective function as a penalty for solutions with large $\Delta\Omega_{\text{op}}$ but small $v_{\text{max,avg}}$. In this paper, we set $\kappa = 0.75$. Considering the high nonlinearity of the problem, we adopt an non-gradient based optimization approach, Genetic Algorithm, to search for the optimum. The key parameters of the genetic algorithm, including population size, mutation rate, crossover rate and Maximum number of iterations, are selected as 20, 0.05, 0.6 and 10, respectively.

The geometry and nonlinear equilibrium path of the *von Mises* truss and the dynamic response of the capsule robot as well as the inner mass in the working frequency domain [10 50] Hz under the excitation force $P_{\text{d}} = 20$ mN are presented in Fig. S14. The net distance G_1 between the mass and front constraint spring locates in the positive stiffness regime, close to the local minimum, as seen in the dished red line in Fig. S14(a). The optimised capsule exhibits a relatively high average speed in a wide frequency band. Compared with the baseline solution (case 3 in Fig. 2 in the main paper), where the net distance locates at $F_{\text{v}} = 0$ and $X_{\text{r}} = H$, the maximum average speed v_{max} increased by 6.29%, and the objective function defined in Eq. (10) increased by 8.09%. As for the case with the maximum average velocity, see the red dot in Fig. S14(b), the inner mass exhibit a periodic response and it only collides with the front constraint spring. The displacement and velocity history diagrams essentially exhibit similar patterns as that in the baseline case, while the inner mass moves much closer to the back constraint spring. The optimised results align with the mechanics we have unveiled from our parametric study.

Note that we introduce an upper limit (penalty) for the working frequency bandwidth in Eq. (10). This penalty is incorporated to prevent the optimizer from converging to solutions with a relatively low speed but a wide effective working frequency band. condition in the objective function. We also conduct the optimisation without the penalty. The configurations of the *von Mises* trusses, along with their nonlinear equilibrium paths using the two different objective functions and the baseline case, are presented in Fig. S15(a, b). The key outputs of the optimisation solution process for objective functions 1 and 2 are presented in Fig. S15(c) and (d), respectively. The dynamic behavior of the capsule robots are shown in Fig. S16. The geometry

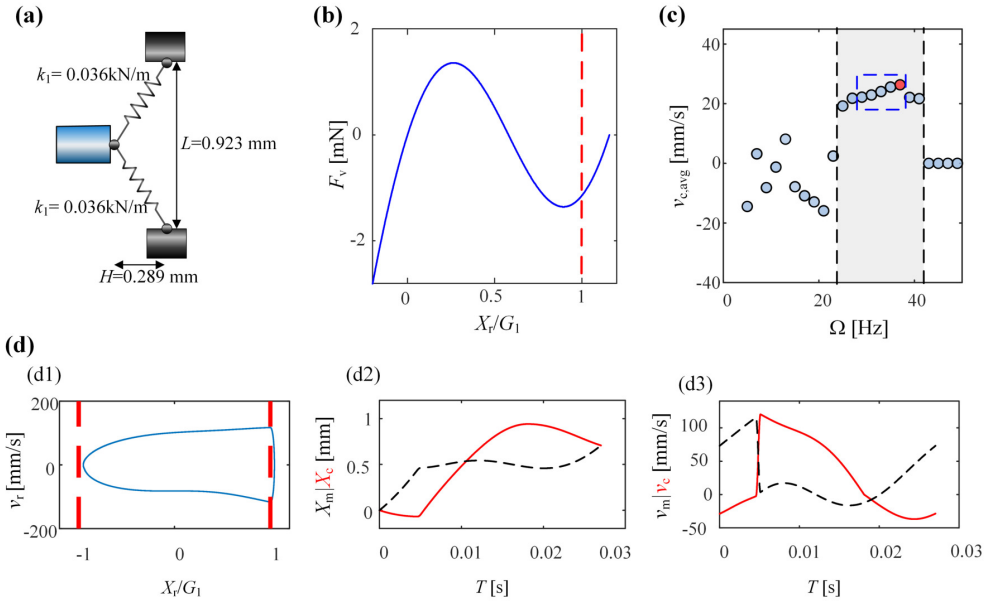

Figure S14: (a) The geometry and the nonlinear equilibrium path of the optimised *von Mises* truss based on the formulation Eq. (10). Note that we set the horizontal spring k_3 as rigid. The blue dashed window encloses the data used for the computation of the objective function. (b) The sensitivity of the average velocity of the capsule robot to excitation frequency under the excitation force $P_\mathrm{d} = 20$ mN. (c) The time history results for the inner mass and the capsule robot for the case with the peak average velocity at $\Omega = 37$ Hz. Subfigures are as described in Fig. S11.

of the two optimized *von Mises* trusses are very similar. Their rise, span, and the stiffness of the inclined springs are almost half of those of the baseline. Accordingly, their structural weight is reduced by 75% and 63%, respectively, compared to the baseline. It's worth noting that the relatively significant drop in structural weight and stiffness leads to a marginal increase in the maximum average speed. Regarding the dynamic behavior of capsules with the fastest propelling speed for each case, their responses are very similar. The only difference is that in the case optimized with penalty in $\Delta\Omega_\mathrm{op}$, the inner mass approaches closer to the back constraint panel in its periodic movement.

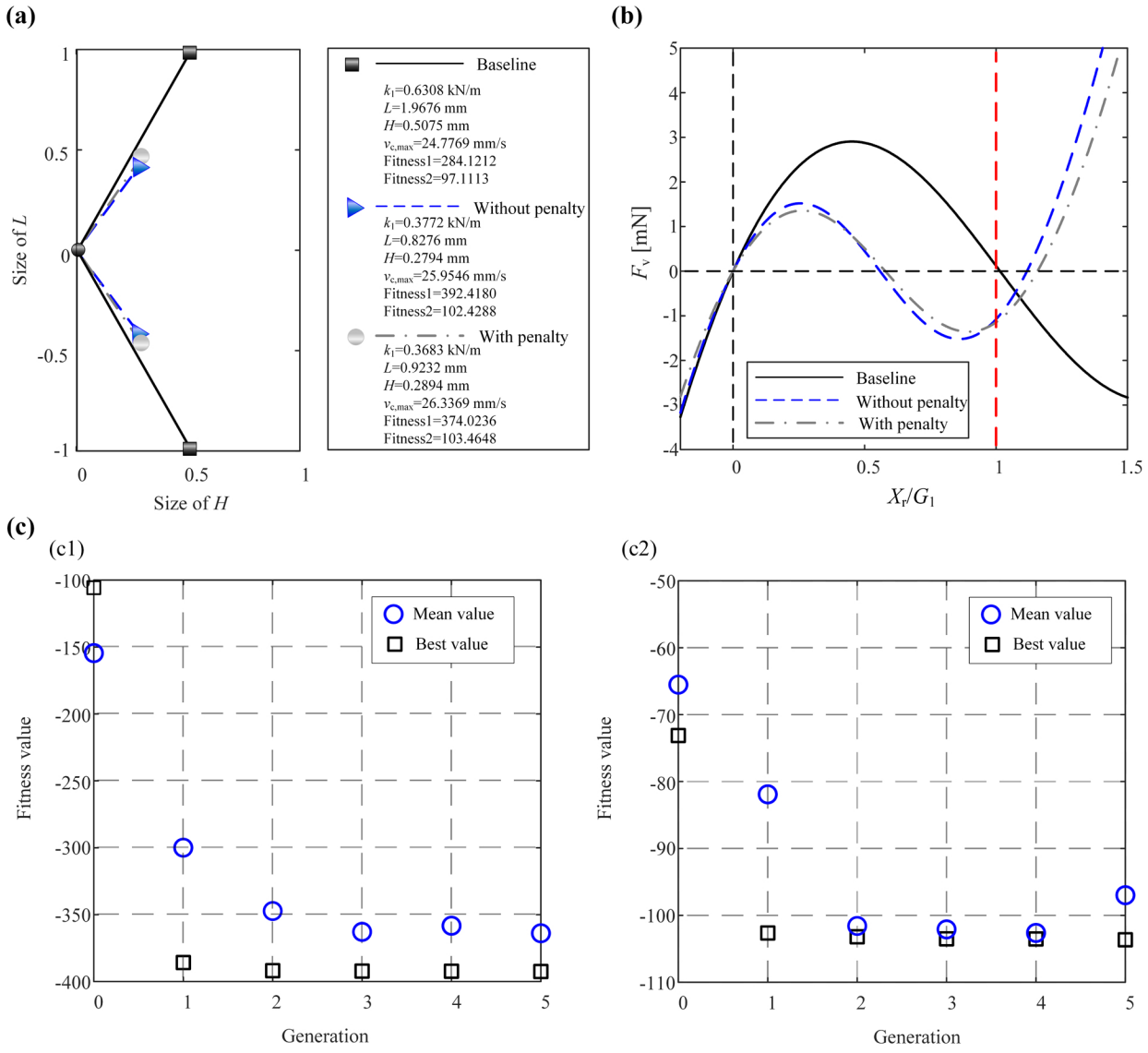

Figure S15: Optimisation results using two different objective functions. (a) The geometric configuration of *von Mises* trusses: the baseline structure, optimised structure with the objective function with and without penalty on the working frequency band $\Delta\Omega_{\mathrm{op}}$, and (b) their load-displacement curve. (c) Curve of fitness with generations in optimization process for two objective functions.

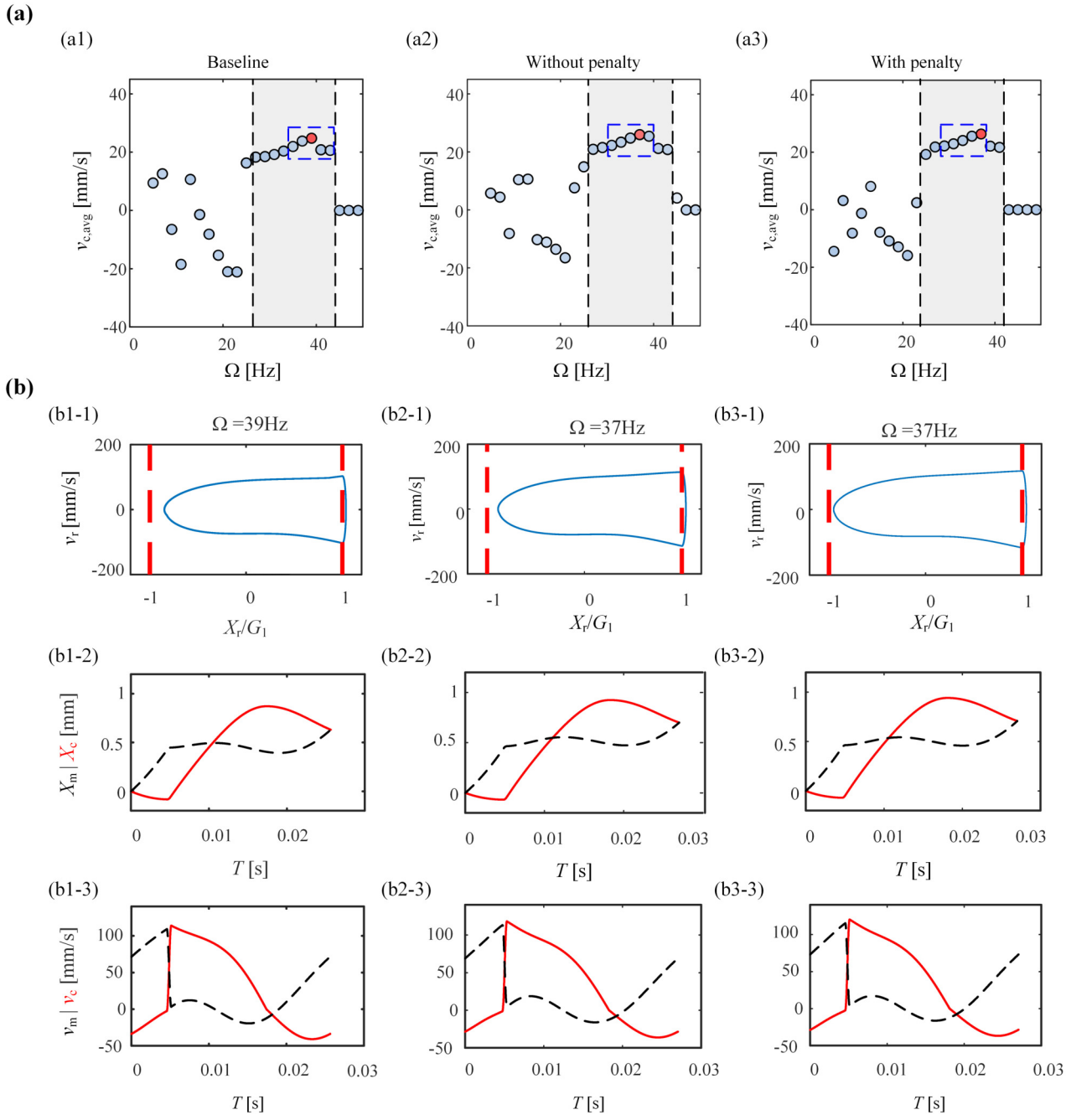

Figure S16: The dynamic response of the capsule robot with the baseline and two optimised *von Mises* springs. The subfigures are as described as those in Fig. S11.

The MATLAB scripts for the objective functions are provided below.

```
% The variable oumigaarr is the frequency sequence
% The variable speedarr is the speed sequence with the frequency in the range of 10-50 Hz
% The variable limit is the lower limit of the acceptable high propelling velocity range
% The variable method is the option variable, which provides two optimization objective functions to choose from.
function [robust]=getrobust(oumigaarr,speedarr,limit,method);
       % find the maximum speed
        [max_sp,max_ind]=max(speedarr);
        % Define labes for the ponits in the acceptable high propelling velocity range as 1, otherwise as 0.
        speed1=speedarr-limit*max_sp;
        jud_1= speed1>0;
        % Find the start of the continuous interval
        if max_ind~=1
            i=max_ind-1;
            while jud_1(i) ==1  && speedarr(i)>0
                if i~=1
                    i=i-1;
                else
                    i=i-1;
                    break;
                end
            end
        % The start of the continuous interval
        start_ind=i+1;
        else
           start_ind=1;
        end
        % Find the end of the continuous interval
        if max_ind ~=size(speedarr,1)
        j=max_ind+1;
        while jud_1(j)==1 && speedarr(j)>0
            if j~=size(speedarr,1)
                j=j+1;
            else
                j=j+1;
                break;
            end
        end
        % The end of the continuous interval
        end_ind=j-1;
        else
            end_ind=size(speedarr,1);
        end
        % Compute the objective function
        if method==1
            o_arr=oumigaarr(start_ind:end_ind);
            s_arr=speedarr2(start_ind:end_ind);
            % Returns the value of the first objective function
            robust=trapz(o_arr,s_arr);
        else
            % If the effective working frequncy band<=5, compute the objective function directly
            if end_ind-start_ind<5
                    o_arr=oumigaarr(start_ind:end_ind);
                    s_arr=speedarr2(start_ind:end_ind);
                    robust=trapz(o_arr,s_arr);
            else
                %If the effective frequency band width is larger than 5, a truncation is required
                runk=0;
                % It is used to record the largest objective function interval
                robumax=0;
                while runk< end_ind-start_ind+1-5+1

                    o_arr=oumigaarr(start_ind+runk:start_ind+5+runk-1);
```

```
                    s_arr=speedarr2(start_ind+runk:start_ind+5+runk-1);
                    robust=trapz(o_arr,s_arr);
                    if robust>robumax
                        robumax=robust;
                    end
                    runk=runk+1;

                end
                robust=robumax;
        end
```

Listing 1: Source script for the objective functions.

References

[1] J. Shen, R. M. J. Groh, M. Schenk, A. Pirrera, Experimental path-following of equilibria using Newton's method. Part I: Theory, modelling, experiments, International Journal of Solids and Structures 210 (2021) 203–223.

[2] R. M. J. Groh, D. Avitabile, A. Pirrera, Generalised path-following for well-behaved nonlinear structures, Comput. Methods Appl. Mech. Eng. 331 (2018) 394–426.

[3] T. Frenzel, C. Findeisen, M. Kadic, P. Gumbsch, M. Wegener, Tailored buckling microlattices as reusable light-weight shock absorbers, Advanced Materials 28 (28) (2016) 5865–5870.

[4] F. Liu, X. Jiang, X. Wang, L. Wang, Machine learning-based design and optimization of curved beams for multistable structures and metamaterials, Extreme Mechanics Letters 41 (2020) 101002.

[5] B. Deng, A. Zareei, X. Ding, J. C. Weaver, C. H. Rycroft, K. Bertoldi, Inverse design of mechanical metamaterials with target nonlinear response via a neural accelerated evolution strategy, Advanced Materials 34 (41) (2022) 2206238.